Proposal for local SAR safety margin in pediatric neuroimaging using 7 T MRI and parallel transmission

N Dudysheva, M Luong, A Amadon, L Morel, N Le Touz, A Vignaud, N Boulant, V Gras

Proposal for local SAR safety margin in pediatric neuro-imaging using 7 T MRI and parallel transmission

N. Dudysheva[1], M. Luong[2], A. Amadon[1], L. Morel[3], N. Le Touz[3], A. Vignaud[1], N. Boulant[1], V. Gras[1]

[1]Université Paris-Saclay, CEA, NeuroSpin, CNRS, BAOBAB, Gif sur Yvette 91191 France
[2]Université Paris-Saclay, CEA, DRF, IRFU, Gif sur Yvette, France
[3]CEA, DAM, CEA-Gramat, F-46500 Gramat, France

Correspondence: Vincent Gras, email: vincent.gras@cea.fr

Abstract

Objective

Ultra-high field MRI with parallel transmission (pTx) provides a powerful neuroimaging tool with potential application in paediatrics. The use of pTx, however, necessitates a dedicated local specific absorption rate (SAR) management strategy, able to predict and monitor the peak local SAR ($pSAR_{10g}$). In this work, we address the $pSAR_{10g}$ assessment for an in-house built 7 T 16Tx32Rx pediatric head coil, using the concept of Virtual Observation Points (VOPs) for SAR estimation.

Approach

We base our study on full-wave electromagnetic simulations performed on a database of 64 numerical anatomical head models of children aged between 4 and 16 years. We built VOPs on different subsets of this database of N=2 up to 30 models, and cross-validated the $pSAR_{10g}$ prediction using non-intersecting subsets, each containing 30 models. We thereby propose a minimum anatomical safety factor (ASF) to apply to the VOP set to enforce safety, despite intersubject variability. Our analysis relies on the computation of the worst case SAR to VOP-SAR ratio, independent of the pTx RF excitation.

Main results

The interpolation model provides that the minimum ASF decreases as $1 + 5.37 \cdot N^{-0.75}$ with N. Using all 64 models to build VOPs leads to an estimated ASF of 1.24 when considering the VOP validity for an infinite number of subjects.

Significance

We propose a general simulation workflow to guide ASF estimation and quantify the trade-off between the number of numerical models available for VOP construction and the safety factor. The approach would apply to any simulation dataset and any pTx setup.

Keywords: radiofrequency power deposition, safety, virtual observation points, ultra-high field, electromagnetic simulation

1. Introduction

Cerebral magnetic resonance imaging at 7 T represents significant progress over 1.5T and 3T MRI due to higher achievable contrast-to-noise (CNR) and signal-to-noise ratios (SNR) (Balchandani *et al* 2015). With the SNR gain invested in image resolution, 7 T MRI increases the visibility of sub-millimeter structures and can enhance the detection of brain lesions. Given the promising results in adults (Bubrick *et al* 2022, Feldman et al 2019, Obusez *et al* 2018), interest in pediatric 7 T MRI is also emerging (Harris *et al* 2016, Lazen *et al* 2024, van der Plas *et al* 2024, Morrison *et al* 2019, Yamada *et al* 2021), and some studies reveal the benefit of ultra-high fields (UHFs) for children's exams, for example, to better detect epileptogenic lesions (Sun *et al* 2018, Vecchiato *et al* 2024, Veersema *et al* 2017).

While the Food and Drug Administration has approved 7 T MR imaging in infants of 1 month and older (FDA 2014), the number of children included in 7 T MRI protocols is still limited (e.g., 3 to 8 subjects aged 7 to 17 years in (Bartolini *et al* 2019, Veersema *et al* 2016, Veersema *et al* 2017, Sun *et al* 2018, and De Ciantis *et al* 2016). Regulatory-approved 7 T MRI systems impose a lower limit of the patient weight of 30 kg (Fagan *et al* 2021, Burkett *et al* 2021, Hangel *et al* 2024), and clinical 7 T MRI studies typically exclude patients younger than 12 years old (Hangel *et al* 2024, van Lanen *et al* 2022). One major hindrance for pediatric UHF MRI is the specific absorption rate (SAR) control needed to limit the deposited RF energy and thus prevent adverse tissue heating (Fiedler *et al* 2018). Some studies address the RF safety at 7 T for neonates (Annink *et al* 2020, Malik *et al* 2021) and children (Malik *et al* 2022) in a single transmit mode, but more comprehensive analysis is still required.

Another limitation of the UHF MRI is a more pronounced inhomogeneity of the transmit radiofrequency (RF) field (Ladd *et al* 2018). Constructive and destructive interferences of the B_1^+ field can lead to local signal hyperintensities in one case and to signal and contrast loss (in particular in temporal lobes and cerebellum) in the other. The problem of B_1^+ heterogeneity is likely to persist in the pediatric population, at least when the head size becomes comparable to the RF wavelength (i.e., for the head diameter greater than 12 cm (Keith *et al* 2024)). In this regard, an efficient solution to fully exploit the potential of UHF MRI is the parallel transmission (pTx) technique, which allows dynamically combining multiple transmit elements to gain control over the effective RF transmission profile (Adriany *et al* 2005, Katscher *et al* 2003). Parallel transmission has demonstrated significant improvement of flip angle homogeneity under energy and SAR constraints for different types of RF excitations (Beqiri *et al* 2018, Gras *et al* 2023, Herrler *et al* 2023, Leitão *et al* 2022, Van Damme *et al* 2021, Yetisir

et al 2022) and promising results in various types of 2D and 3D MR acquisitions to detect brain malformations in adults (metastases, epilepsy, multiple sclerosis, etc.) (Alushaj *et al* 2024, Duan *et al* 2023, Herrler *et al* 2021, Hillyer *et al* 2023, Klodowski *et al* 2024).

In pTx mode, local SAR control becomes more challenging due to a changeable pattern of the transmitted EM field. To our knowledge, the SAR supervision with corresponding safety margins for pTx exams have only been established for adults. A dedicated study therefore must be carried out to enable the reliable local SAR control on children. In this work, we address this question by focusing on the school aged population (age > 6 years), where the brain volume is close to reaching its maximum but the body size and the head anatomy is still evolving significantly. In this case, we expect the B_1^+ heterogeneity of the circularly polarized (CP) mode to be problematic at 7 T, and the pTx hardware to remain a valuable tool to solve this problem while the actual $pSAR_{10g}$ may deviate from that predicted using the adult standard.

To date, the gold standard approach for the SAR evaluation in MRI relies on 3D electromagnetic simulation on a numerical model (NM) of the head and the torso and on a detailed model of the transmitting RF coils and the environment (scanner's inner bore, patient table) (Fiedler *et al* 2018, Wolf *et al* 2013). Doing this, one must keep in mind that the electric field and thus the SAR distribution vary with the head anatomy, its position in the coil, and the dielectric properties of the tissues (Bottauscio *et al* 2024, de Greef *et al* 2013, Goren *et al* 2024, Kopanoglu *et al* 2020, Shao *et al* 2015). Therefore, for the SAR simulations to be representative of the experimental SAR during in vivo studies, the simulations must cover as much as possible the above source uncertainties (Le Garrec *et al* 2017, Meliadò *et al* 2020). This can be done in practice by performing the SAR simulations across a variety of NMs and by estimating a suitable safety margin on the SAR simulation. The larger the simulation database, the more accurate will be the statistical description of the SAR and the more educated the safety margin calculation will be (Ipek *et al* 2014, Destruel *et al* 2024). This approach is especially important in the context of pediatric imaging given that the anatomy of the head, and in particular its size, continues to evolve up to adulthood (Chirita-Emandi *et al* 2015, Rollins *et al* 2010), while the brain after 6 years reaches about 95% of the adult brain volume (Caviness *et al* 1996, Lenroot *et al* 2006) continuing a slight expansion (Matsuzawa *et al* 2001). Furthermore, for pediatric SAR control, it may be inappropriate to scale available adult head models, as the children's head morphology and proportions differ from the adult case (Bartholomeusz *et al* 2002, Christ and Kuster 2005, Júlíusson *et al* 2013, Myer 1995), and dedicated databases are possibily needed.

For a single-transmit coil (sTx), the local SAR to global SAR ratio being independent of the RF excitation, its analysis for different numerical models directly provides information on the inter-subject SAR variability, and subsequently on the required safety margin. For a parallel transmit coil array, the problem yet is much more complex as the local SAR distribution depends on the applied RF waveforms (Seifert *et al* 2007, Graesslin *et al* 2012), making the SAR variations due to anatomical variability and RF excitation tightly intricate. To extend the statistical analysis of the SAR in pTx, it is necessary to recall the strategy for monitoring the local SAR. In this case, a collection of matrices called Virtual Observation Points (VOPs) (Eichfelder *et al* 2011) constructed among a series of numerical models delivers a conservative estimation of the maximum local SAR – the so-called VOP-SAR. Therefore, for a rigorous analysis of the SAR variability, the safety relevant parameter in pTx is the ratio of the actual peak local SAR to VOP-SAR, calculated from the numerical models. As this ratio depends on the pTx RF excitation, and as this excitation can be chosen freely, we are here interested more specifically in the maximum value this ratio takes when exploring all pTx RF excitations (Gras *et al* 2024). With this approach, like in sTx, it is theoretically possible – the potential difficulties to compute the worst-case local SAR to VOP-SAR ratio put aside – to study the effect of anatomical variations on the SAR prediction independently of the applied pTx RF excitation. The quantity of interest is then the risk to underestimate the peak local SAR given an arbitrary subject with the VOPs computed over a limited set of numerical models.

In this work, we conduct a numerical study of the pTx local SAR control on a home-built database called VARDAS consisting of 64 numerical head models of children aged from 4 to 16 years (Delbany *et al* 2022) and for an in-house built 16Tx32Rx head coil called Avanti2 (Luong *et al* 2022). This analysis represents part of the work aimed at conducting clinical examinations in children of a similar age range (6 years is considered the lower limit in our future study for standing still inside the scanner for 30 min without sedation).

We first detail the methodology for assessing the safety of a given VOP set on distinct numerical test models using a numerically tractable estimation of the worst-case local SAR to VOP-SAR ratio, the latest called the R criterion (Gras *et al* 2024). Based on it, we introduce a simple VOP safety condition as $R<1$ and define the R map as the R value at each voxel of a test model. We derive two SAR safety metrics, one corresponding to the maximum of the R-map and the second based on the mass of voxels where the R-map exceeds 1. We show that these metrics provide relevant measure of the necessary VOP safety margins. Taking advantage of the variety of NMs in the VARDAS database, we performed a numerical study of the safety

margins needed to encompass the inter-subject SAR variability for the Avanti2 head coil array and for scanning children above 6 years of age. We provide an analysis of the minimum required anatomical safety factors (ASF) as a function of the number of NMs available to compute the VOPs. A preliminary account of this work was given during the 2024 ISMRM conference (Dudysheva *et al* 2024).

2. Theory

2.1. Local SAR monitoring in pTx

Let N_{ch} denote the number of Tx-channels of the transmit array, $\mathbf{E}(\boldsymbol{r}) \in \mathbb{C}^{3\times N_{\mathrm{ch}}}$ – the electric field profiles (the j^{th} column of this matrix providing the *x*, *y* and *z* components of the E-field created at $\boldsymbol{r}$ for 1 W available input power on port *j*), $\sigma(\boldsymbol{r})$ – the electrical conductivity and $\rho(\boldsymbol{r})$ – the tissue density. Let also τ be the SAR averaging time and $\boldsymbol{w}$ represent the continuously defined RF waveform within a sliding temporal window of duration τ; here, $\boldsymbol{w}(\mathrm{t}) \in \mathbb{C}^{N_{\mathrm{ch}}}$ (in $\sqrt{\mathrm{W}}$) can be zero, e.g., beyond the RF pulses applied. Then, the SAR averaged over the temporal window and the local spatial region $\upsilon(\boldsymbol{r})$ around a point $\boldsymbol{r}$ can be expressed as (Seifert *et al* 2007):

$$\mathrm{SAR}(\boldsymbol{r},\boldsymbol{w}) = \frac{1}{\tau}\int_{\mathrm{t}'=0}^{\tau} \boldsymbol{w}(\mathrm{t}')^{\mathrm{H}} \left(\frac{1}{|\boldsymbol{v}(\boldsymbol{r})|} \int_{\boldsymbol{r}'\in\boldsymbol{v}(\boldsymbol{r})} \mathbf{E}(\boldsymbol{r}')^{\mathrm{H}} \frac{\sigma(\boldsymbol{r}')}{2\rho(\boldsymbol{r}')} \mathbf{E}(\boldsymbol{r}) \mathrm{d}^3\boldsymbol{r}' \right) \boldsymbol{w}(\mathrm{t}')\, \mathrm{dt}' \qquad (1)$$

where $\cdot^{\mathrm{H}}$ designates the Hermitian conjugation operator and $|\boldsymbol{v}(\boldsymbol{r})|$ denotes the volume. As the sliding window progresses over time, the RF waveform $\boldsymbol{w}$ within it changes and may take any temporal shape.

Safety standards (IEC 2010) prescribe to consider the local SAR averaged over the volume $\upsilon_{10\mathrm{g}}(\boldsymbol{r})$ corresponding to 10g of tissue and the temporal sliding window with a duration τ of 6 min and 10 s. Defining the 10 g SAR matrix in $\boldsymbol{r}$ (positive definite), $\mathbf{Q}(\boldsymbol{r})$, as the spatial averaging of $\mathbf{E}^{\mathrm{H}}\frac{\sigma}{2\rho}\mathbf{E}$ over $\upsilon_{10\mathrm{g}}(\boldsymbol{r})$ (IEEE 2002), $\mathrm{SAR}(\mathbf{Q}(\boldsymbol{r}),\boldsymbol{w})$ becomes the temporal average of $\boldsymbol{w}^{\mathrm{H}}\mathbf{Q}(\boldsymbol{r})\boldsymbol{w}$. As $\mathbf{Q}(\boldsymbol{r})$ is independent of the pTx waveforms, it can be precomputed on numerical models and used routinely for SAR evaluation for any given excitation $\boldsymbol{w}$.

Monitoring the local SAR in pTx would then consist in controlling its value simultaneously across all positions in the head ($\boldsymbol{r} \in \boldsymbol{\mathcal{V}}$) continuously over time. Due to the prohibitive number of $\mathrm{SAR}_{10\mathrm{g}}$ evaluations that this would imply – over ~10^5 to sample correctly the SAR relevant region of interest $\boldsymbol{\mathcal{V}}$ – it is advantageous to replace the exact maximum local

SAR estimation $\max_{\boldsymbol{r}\in\boldsymbol{\mathcal{V}}}\mathrm{SAR}(\mathbf{Q}(\boldsymbol{r}),\boldsymbol{w})$ with a *conservative* estimation thereof e.g. of the form $\max_{\boldsymbol{r}\in\boldsymbol{\mathcal{V}}^*}(\mathrm{SAR}(\mathbf{Q}(\boldsymbol{r})+\delta\,\mathbf{I},\boldsymbol{w})$ using a smaller number of matrices from $\boldsymbol{\mathcal{V}}^*$. Here, $\delta>0$ is a parameter allowing for a tradeoff between compression ratio ($\mathrm{card}(\boldsymbol{\mathcal{V}}^*)/\mathrm{card}(\boldsymbol{\mathcal{V}})$) and SAR_{10g} overestimation (Eichfelder *et al* 2011) and $\mathbf{I}$ is the identity matrix. The matrices $\boldsymbol{\mathcal{Q}}^* \coloneqq \{\mathbf{Q}(\boldsymbol{r})+\delta\,\mathbf{I},\boldsymbol{r}\in\boldsymbol{\mathcal{V}}^*\}$ are called the VOP matrices, and the maximum SAR_{10g} across them

$$\mathrm{SAR}^*(\boldsymbol{\mathcal{Q}}^*,\boldsymbol{w}) \coloneqq \max_{\mathbf{Q}^*\in\boldsymbol{\mathcal{Q}}^*}\mathrm{SAR}(\mathbf{Q}^*,\boldsymbol{w}) \tag{2}$$

is hereafter called the VOP-SAR. The fact that the VOP matrices provide a conservative estimation of the local SAR imply the so-called domination criterion:

$$\mathrm{SAR}(\mathbf{Q}(\boldsymbol{r}),\boldsymbol{w}) \le \mathrm{SAR}^*(\boldsymbol{\mathcal{Q}}^*,\boldsymbol{w})\ \forall\,\boldsymbol{r},\boldsymbol{w}. \tag{3}$$

2.2. VOP safety test

Let $\boldsymbol{\mathcal{Q}}^*$ be a "candidate" VOP set for which we would like to test the domination criterion on some SAR matrix $\mathbf{Q}$. Let us define the R-criterion $\mathrm{R}(\mathbf{Q},\boldsymbol{\mathcal{Q}}^*)$ as the worst-case local SAR to VOP-SAR ratio considering all possible RF waveforms $\boldsymbol{w}$:

$$\mathrm{R}(\mathbf{Q},\boldsymbol{\mathcal{Q}}^*) \coloneqq \max_{\boldsymbol{w}}\left(\frac{\mathrm{SAR}(\mathbf{Q},\boldsymbol{w})}{\mathrm{SAR}^*(\boldsymbol{\mathcal{Q}}^*,\boldsymbol{w})}\right). \tag{4}$$

Since the condition $\mathrm{R}(\mathbf{Q},\boldsymbol{\mathcal{Q}}^*)\le 1$ signifies that the VOP-SAR upper bounds the actual SAR_{10g} for any time-varying $\boldsymbol{w}$, it is equivalent to the domination condition (Eq. 3). In Gras *et al* 2024, it is shown that $\mathrm{R}(\mathbf{Q},\boldsymbol{\mathcal{Q}}^*)$ can be obtained numerically without resorting to time-consuming and inaccurate Monte-Carlo simulations, by solving the following convex optimization problem in $\mathbb{R}^{2N_{\mathrm{ch}}}$:

$$\mathrm{R}(\mathbf{Q},\boldsymbol{\mathcal{Q}}^*) = \max_{\boldsymbol{v}\in\mathbb{C}^{N_{\mathrm{ch}}}}\left(\frac{\boldsymbol{v}^{\mathrm{H}}\mathbf{Q}(\boldsymbol{r})\boldsymbol{v}}{\max_{\mathbf{Q}^*\in\boldsymbol{\mathcal{Q}}^*}(\boldsymbol{v}^{\mathrm{H}}\mathbf{Q}^*\boldsymbol{v})}\right) = \max_{\boldsymbol{v}\in\mathbb{C}^{N_{\mathrm{ch}}}}(\boldsymbol{v}^{\mathrm{H}}\mathbf{Q}(\boldsymbol{r})\boldsymbol{v})\ \text{s.t.}\ \boldsymbol{v}^{\mathrm{H}}\mathbf{Q}^*\boldsymbol{v}\le 1\ \text{for all}\ \mathbf{Q}^*\in\boldsymbol{\mathcal{Q}}^* \tag{5}$$

This way, it was shown that testing the domination condition independently of the RF excitation is computationally feasible. According to Eq. 5, the subsequent analysis does not have to consider all possible time-varying RF waveforms ($\boldsymbol{w}$), but only so-called static RF shims ($\boldsymbol{v}$). We note also that scaling the VOPs with a factor k decreases R by the same factor:

$$\frac{1}{\mathrm{k}}\mathrm{R}(\mathbf{Q}(\boldsymbol{r}),\boldsymbol{\mathcal{Q}}^*) = \mathrm{R}(\mathbf{Q}(\boldsymbol{r}),\mathrm{k}\boldsymbol{\mathcal{Q}}^*). \tag{6}$$

As a consequence, the R-criterion can be used to compute the minimum safety factor to apply on the VOP matrices to meet the domination condition ($\mathrm{R}\le 1$) considering a candidate set of VOPs and a complementary set of head models to test.

For a given test anatomical model $\mathcal{M}_{\mathrm{TEST}}$, the associated ROI $\boldsymbol{\mathcal{V}}_{\mathrm{TEST}}$, and SAR matrices $\boldsymbol{\mathcal{Q}}_{\mathrm{TEST}} = \{\mathbf{Q}_{\mathrm{TEST}}(\boldsymbol{r}) | \, \boldsymbol{r} \in \boldsymbol{\mathcal{V}}_{\mathrm{TEST}}\}$, we defined the R-map as the mapping of the R-criterion across all positions in $\boldsymbol{\mathcal{V}}_{\mathrm{TEST}}$:

$$\mathrm{Rmap}(\mathcal{M}_{\mathrm{TEST}}, \boldsymbol{\mathcal{Q}}^*, \boldsymbol{r}) \coloneqq \mathrm{R}(\mathbf{Q}_{\mathrm{TEST}}(\boldsymbol{r}), \boldsymbol{\mathcal{Q}}^*), \tag{7}$$

and subsequently the Rmax and RiskMass metrics as:

$$\mathrm{Rmax}(\mathcal{M}_{\mathrm{TEST}}, \boldsymbol{\mathcal{Q}}^*) \coloneqq \max_{\boldsymbol{r} \in \boldsymbol{\mathcal{V}}_{\mathrm{test}}} \mathrm{Rmap}(\mathcal{M}_{\mathrm{TEST}}, \boldsymbol{\mathcal{Q}}^*, \boldsymbol{r}), \tag{8}$$

$$\mathrm{RiskMass}(\mathcal{M}_{\mathrm{TEST}}, \boldsymbol{\mathcal{Q}}^*) \coloneqq \mathrm{card}(\{\boldsymbol{r} \in \boldsymbol{\mathcal{V}};\ \mathrm{Rmap}(\mathcal{M}_{\mathrm{TEST}}, \boldsymbol{\mathcal{Q}}^*, \boldsymbol{r}) > 1\}) \cdot \delta\mathrm{V} \cdot \rho, \tag{9}$$

where δV is the voxel volume, and ρ is the tissue density. The Rmax metric reflects the worst-case local SAR to VOP-SAR ratio attainable in $\boldsymbol{\mathcal{V}}_{\mathrm{test}}$, while RiskMass quantifies the portion of $\boldsymbol{\mathcal{V}}_{\mathrm{test}}$ with a risk to underestimate the SAR, still in the $\boldsymbol{w}$(t) worst case scenario. The definition of these metrics can finally be generalized to a multiplicity M of test models $\boldsymbol{\mathcal{G}}_{\mathrm{TEST}} = \{\mathcal{M}_{\mathrm{TEST},1}, \cdots, \mathcal{M}_{\mathrm{TEST},M}\}$ by computing the maximum of Rmax and RiskMass across all of them:

$$\mathrm{gRmax}(\boldsymbol{\mathcal{G}}_{\mathrm{TEST}}, \boldsymbol{\mathcal{Q}}^*) \coloneqq \max_{j=1..M} \mathrm{Rmax}\left(\mathcal{M}_{\mathrm{TEST},j}, \boldsymbol{\mathcal{Q}}^*\right) \tag{10}$$

$$\mathrm{gRiskMass}(\boldsymbol{\mathcal{G}}_{\mathrm{TEST}}, \boldsymbol{\mathcal{Q}}^*) \coloneqq \max_{j=1..M} \mathrm{RiskMass}\left(\mathcal{M}_{\mathrm{TEST},j}, \boldsymbol{\mathcal{Q}}^*\right) \tag{11}$$

The VOP set is finally said to be safe with respect to $\boldsymbol{\mathcal{G}}_{\mathrm{TEST}}$ if $\mathrm{gRmax}(\boldsymbol{\mathcal{G}}_{\mathrm{TEST}}, \boldsymbol{\mathcal{Q}}^*) \leq 1$, or equivalently $\mathrm{gRiskMass}(\boldsymbol{\mathcal{G}}_{\mathrm{TEST}}, \boldsymbol{\mathcal{Q}}^*) = 0$.

2.3. VOP anatomical safety margins

If the domination condition (Eq. 3) is violated, it is sufficient to scale the VOPs with some factor k (i.e. replace $\boldsymbol{\mathcal{Q}}^*$ by $\boldsymbol{\mathcal{Q}}^{**} \coloneqq \{k\mathbf{Q}^*; \mathbf{Q}^* \in \boldsymbol{\mathcal{Q}}^*\}$) to enforce the VOP safety condition with respect to test models. According to Eq. 6, the minimum scaling coefficient, or strict anatomical safety factor (sASF), is given by:

$$\mathrm{sASF} \coloneqq \mathrm{gRmax}(\boldsymbol{\mathcal{G}}_{\mathrm{TEST}}, \boldsymbol{\mathcal{Q}}^*). \tag{12}$$

Further, we consider a relaxed safety factor rASF ≤ sASF as the minimal factor such that the following two conditions are satisfied:

$$\mathrm{gRiskMass}(\boldsymbol{\mathcal{G}}_{\mathrm{TEST}}, \mathrm{rASF} \cdot \boldsymbol{\mathcal{Q}}^*) \leq 1\mathrm{g} \tag{13a}$$

$$\mathrm{gRmax}(\boldsymbol{\mathcal{G}}_{\mathrm{TEST}}, \mathrm{rASF} \cdot \boldsymbol{\mathcal{Q}}^*) \leq 2 \tag{13b}$$

In this way, one can tolerate that the VOP matrices fail to overestimate the $\mathrm{SAR}_{10\mathrm{g}}$ in the worst-case scenario of RF excitation, but only in a small number of voxels (the associated mass of

tissue does not exceed 1g) and still with the constraint that $R < 2$ (maximum twofold SAR_{10g} underestimation in this small portion is accepted). We note that rASF can be determined numerically by dichotomy through scaling the Rmap by an appropriate coefficient and directly recalculating gRiskMass and gRmax.

2.4. VOP construction

As shown in Gras *et al* 2024, it is advantageous to also use the R-criterion to compute VOPs. In this work, we exploit a variant of the "CO" (convex optimization) algorithm proposed in Gras *et al* 2024, where the SAR matrices are reordered according to the R-criterion in each iteration of the algorithm. Let $\boldsymbol{\mathcal{Q}}$ be the set of SAR matrices to compress, $\boldsymbol{\mathcal{Q}}^*$ be the growing set of VOP matrices, and $\boldsymbol{\mathcal{Q}}_{\text{remain}} \subset \boldsymbol{\mathcal{Q}}$ be the set of SAR matrices that remain to be classified. Within one iteration of the algorithm, we compute $R(\boldsymbol{\mathcal{Q}}^*, \mathbf{Q})$ criterion for all SAR matrices $\mathbf{Q}$ in $\boldsymbol{\mathcal{Q}}_{\text{remain}}$. We then 1) eliminate the SAR matrices satisfying $R(\boldsymbol{\mathcal{Q}}^*, \mathbf{Q}) \leq 1$ (matrices that turn out to be already dominated), and 2) integrate into $\boldsymbol{\mathcal{Q}}^*$ the SAR matrix returning the highest R (referred to as maxR). At each step, the number of VOPs increases by one. At the same time, the number of non-dominated $\boldsymbol{\mathcal{Q}}_{\text{remain}}$ decreases by at least one element until this set is empty. In contrast with the "CO" algorithm, to control the maximum number of VOPs, we allow stopping the iteration process before the condition $\text{maxR} = 1$ is met, and then use Eq. 6 with k=maxR to enforce VOP domination for all the $\boldsymbol{\mathcal{Q}}$. A diagram of this variant of the CO algorithm is provided in Supplementary Information S1.

3. Methods

In the following, we exploit a database of head NMs to derive the strict and relaxed anatomical safety factors. We first describe this database, the RF coil model used for this study and the 3D full-wave electromagnetic simulations providing the corresponding 10-g SAR matrices. We then present the methodology to determine the anatomical safety margins, and to investigate their variations with the number of models used to compute VOP matrices.

3.1. The "VARDAS" database

The VARDAS database used for this study provides 64 numerical head models of human subjects aged from 4 to 15 years (see the age and weight distributions in Fig. 1). This database was created from 1-mm resolved T_1-weighted acquisitions (TR=2300 ms, TI=900 ms, TE=4.18 ms, FA=9°) performed on a 3T Trio MRI scanner (Siemens Medical Solutions, Germany) between February 2011 and November 2019 (Delbany *et al* 2022). As the MRI

images of this database did not extend to the shoulders, a uniform "reference" neck and shoulders model (dielectric properties of the skeletal muscles) was merged with each head

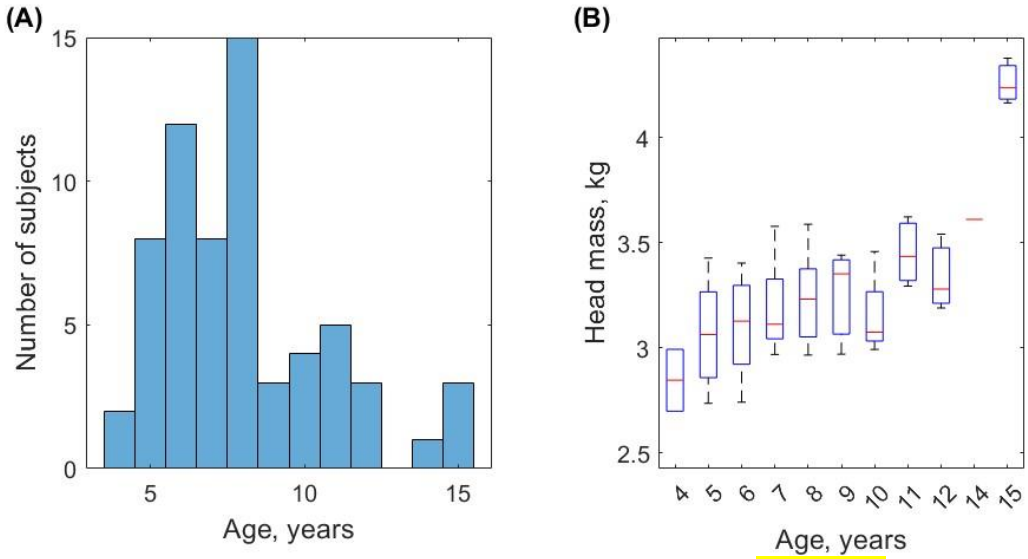

Figure 1. Characteristics of the VARDAS database containing numerical head models of children from 4 to 15 years old (64 subjects in total): (A) age distribution, (B) head mass versus age.

model after proper scaling to adapt it to the head size. The transition plane was positioned in the neck area, at the level of the fifth cervical.

Each MRI anatomical image was segmented (see a segmentation example in Fig. 2) in the 9 compartments, for which the average dielectric properties were prescribed (Gabriel *et al* 1996), as presented in Table I. We used first the segmentation tool of SPM to identify the cerebrospinal fluid (CSF), the brain, and non-brain tissue (skin, torso, fat, and bone), and the air volumes. Using fixed T_1 contrast thresholds, we then partitioned the brain mask in a white mater (WM) and a grey matter (GM) regions and with the skull mask, we separated fat and non-fat regions. Additionally, we marked the left and right eyeball, the course of the trachea, and the spinal cord. These added geometric priors were necessary to improve the segmentation as one limitation of the available data was the lack of the UTE contrast for bone detection and T_2 contrast for CSF detection. Each model was positioned in the head coil with the gravity center of the brain matched with the coil center. Manual adjustment of the final position was allowed to ensure that the head did not intersect the coil's helmet.

Table I. Physical properties of different head regions of numerical models used in the VARDAS database. WM: white matter; GM: grey matter; CSF: cerebrospinal fluid.

	WM	**GM**	**CSF**	**eye**	**fat**	**skin**	**bone**	**torso**	**air**

ε_r	43.8	43.8	72.8	69.0	5.63	49.9	13.4	58.2	1
σ (S/m)	0.41	0.41	2.22	1.52	0.04	0.64	0.08	0.77	0

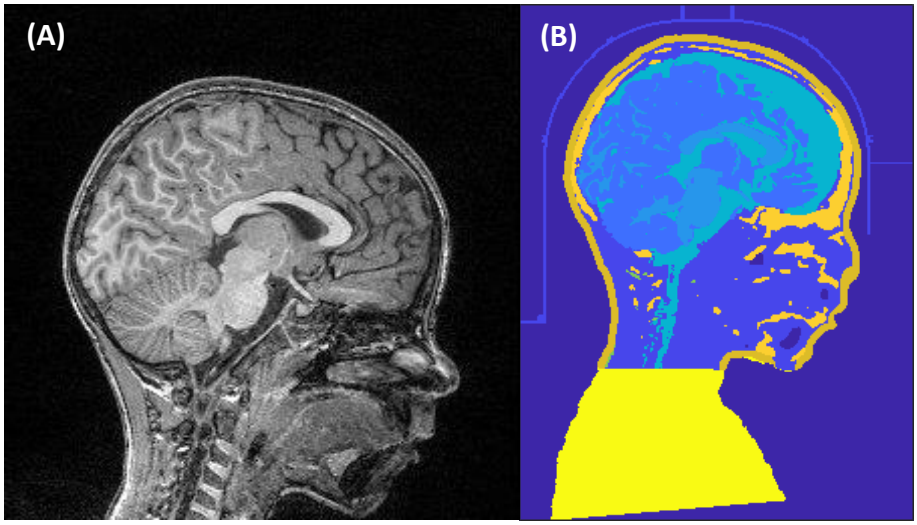

Figure 2: (A) 3T MRI image (T_1-w,1 mm^3) of one subject (4 year-old, height 1.09 m, weight 17 kg), (B) obtained numerical head model (see tissue classes in Table I) extended with the reference "neck and shoulder" model and positioned in the coil.

3.2. The Avanti2 RF coil design

The Avanti2 head coil is a home-made 16Tx32Rx array, which can be used in combination with a local B_0 shimming array (Pinho *et al* 2022). This implied several constraints on the design, in particular on the 27cm-outer diameter of the device to fit inside the local shim

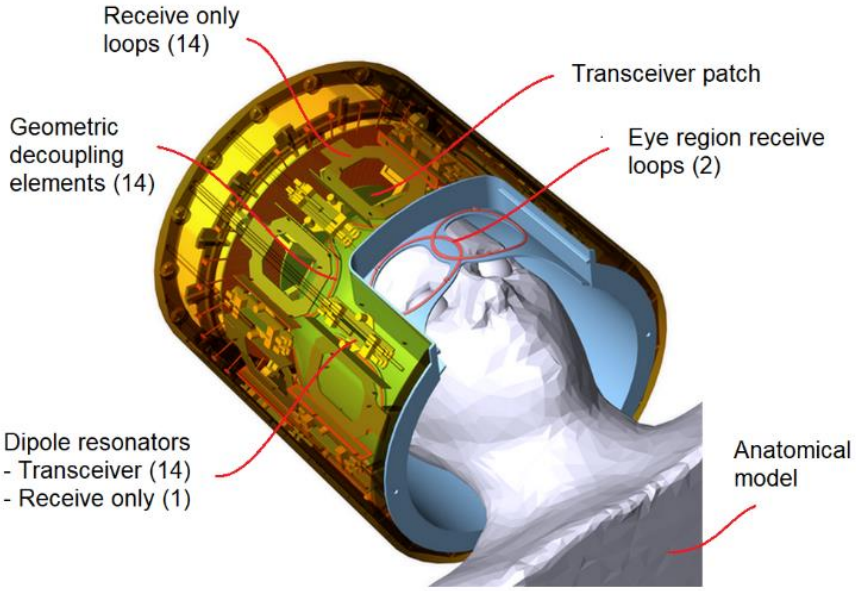

Figure 3. Design of the Avanti2 16Tx32Rx array. This coil array is composed of two rows of linear resonators (7 in the lower row, 8 in the upper row), one patch antenna on the top of the head and 16 loops forming a receive-only array.

array. The Avanti2 RF coil is composed of 15 linear resonators (the said “dipoles”) arranged in a lower and upper row in feet-head direction, and one patch resonator located at the top (see Fig. 3). These resonators are used as transmitters and receivers. It also comprises a set of 16 receive-only loops. The dipoles and the patch resonator were tuned by geometric deformation of the conducting surfaces and their input impedance matched by adjusting the size of the coupling loop and center position of the feeding connection on the patch. In this design, all resonators are tuned and matched to 50 Ω, and 50 Ω input impedance and noise-matched preamplifiers are considered (NF=0.6 dB typically). In order to use the Avanti2 head coil on a parallel 8Tx system, the so-called F2FH Tx channel combination was used. In F2FH, two face-to-face dipoles with respect to the sagittal plane were paired. A detailed description of the coil design, which was developed for 7T and 11.7T MRI brain imaging, is provided in (Luong *et al* 2022).

3.3. SAR simulation

Full-wave electromagnetic simulations were performed using GORF (Pecqueux and Labarbe 2016), an in-house developed finite difference time domain (Taflove *et al* 2003) electromagnetic solver of DAM/CEA, Gramat, France. The simulation volume was 660x660x720 mm, and contained a 600-mm diameter perfectly conduction cylinder to model the inner bore of the magnet, a simple model of the patient table, the transmit architecture of the Avanti2 head coil and the head and neck+shoulders model. The 16-channel receive array was not taken into account in the electromagnetic modeling. We included a perfectly matched layer model at the boundaries of the simulation volume; the Yee cell dimension was $(1\ \text{mm})^3$.

For each head model, we ran 17 independent simulations (1 per dipole and two for the patch antenna, the latter being seen as a 2-port structure, these two ports being driven in quadrature) wherein one port was connected to a unit power source and all the others were terminated by a 50 Ω resistor. After Fourier transform of the simulation data, we reconstructed 17 electric (E) and 17 magnetic (H) field maps defined on a 1-mm resolved grid. The electric field maps were then processed in Matlab (R2022b) to compute the SAR matrices and subsequently, using a low-pass spatial filter, the 10g-averaged SAR matrices. To reduce the size of the processed data, we decreased the resolution of the 10g-SAR Q-matrix maps to $(2\ \text{mm})^3$.

Identical SAR simulations were also performed on Thelonius (6 years old boy, height 1.15 m, weight 18.6 kg) and Billie (11 years old girl, height 1.49 m, weight 34 kg) models of the “Virtual Family” v 2.0.1 (Gosselin *et al* 2014).

The validity of the electromagnetic simulations was tested on a 16cm-diameter spherical phantom filled with agarose with measured dielectric constants $\varepsilon_r = 72$ and conductivity at 300 MHz $\sigma = 0.8$ S/m. Using this phantom, we first checked the agreement between the measured (2D sat-TurboFLASH sequence in interferometric mode (Amadon *et al* 2012), 5 mm isotropic) B_1^+ profiles ($\boldsymbol{b}_{1,\mathrm{meas}}(\boldsymbol{r}) \in \mathbb{C}^8$) and the simulated ones ($\boldsymbol{b}_{1,\mathrm{sim}}(\boldsymbol{r}) \in \mathbb{C}^{17}$). We additionally compared an MR thermometry-based temperature rise (PRF method, 10-min heating with CP mode-equivalent RF shim with total output power of 32 W) with the simulation (thermal diffusion equation with the SAR acting as a heating source) (Zanche *et al* 2022, Boulant *et al* 2018). For those comparisons involving actual measurements on the scanner with 8 transmit B_1^+ field maps, we calibrated the simulations by applying the experimentally fitted F2FH coil combination $\mathbf{L}_{\mathrm{cal}} \in \mathbb{C}^{8\times 17}$ that minimized the residual difference between $\boldsymbol{b}_{1,\mathrm{meas}}(\boldsymbol{r})$ and $\mathbf{L}_{\mathrm{cal}}\boldsymbol{b}_{1,\mathrm{sim}}(\boldsymbol{r})$. The results are reported in Supplementary Information S2 to S4.

In this work, we additionally considered the modelling inaccuracies or uncertainties (Boulant et al 2018) by adding to the 10g SAR matrices a matrix $\Lambda\|\mathbf{Q}\|_2 \cdot \mathbf{I}$ with $\Lambda > 0$, i.e. each SAR matrix $\mathbf{Q}$ was replaced with

$$\mathbf{Q} + \Lambda \|\mathbf{Q}\|_2 \mathbf{I}. \tag{14}$$

This additive term naturally preserves the Hermitian symmetry of the SAR matrix and necessarily increases the estimated SAR_{10g} based on the total incident power and the amount of E-field contained in the $\mathbf{Q}$ matrix. Based also on the comparison between simulated and measured transmit B_1 fields, a factor $\Lambda = 0.1$ was deemed sufficient to account for the simulation inaccuracies in our analysis (see Supplementary Information S6).

3.4. Numerical study

The numerical study was performed on the 64 NMs to compute the strict and relaxed ASFs as a function of the number of NMs used for VOP construction. First, a VOP basis of N NMs, $\boldsymbol{\mathcal{G}}_{\mathrm{VOP}_N} = \{\mathcal{M}_1, \cdots, \mathcal{M}_N\}$, is selected to construct a set of VOP matrices $\boldsymbol{\mathcal{Q}}_N^* := \boldsymbol{\mathcal{Q}}^*(\boldsymbol{\mathcal{G}}_{\mathrm{VOP}_N})$ on the corresponding simulations. Second, we choose a non-intersecting *test basis* $\boldsymbol{\mathcal{G}}_{\mathrm{TEST}}$ of M=30 models, and test $\boldsymbol{\mathcal{Q}}_N^*$ on them (see Fig. 4 for a graphical view of the workflow). The test basis size was set equal to 30, i.e. about half the size of the database. Finally, we determine the anatomical safety factors (Eq. 12 and 13) to be applied to the VOPs to enforce their safety with respect to $\boldsymbol{\mathcal{G}}_{\mathrm{TEST}}$. This analysis is performed for N=2…30 (7 different values were considered), and is repeated 15 times for each N value (each time with a new VOP basis – test basis pair). The models in $\boldsymbol{\mathcal{G}}_{\mathrm{VOP}_N}$ and $\boldsymbol{\mathcal{G}}_{\mathrm{TEST}}$ were randomly selected from the entire database across

different age subgroups to span as much as possible the age distribution. Overall, 105 VOP sets (N values × 15 repetitions) were constructed and tested on 105 distinct test groups.

For the VOP construction, we adopted the following two-stage compression (its schema is presented in Supplementary Information S5). First, model-specific VOPs, $\boldsymbol{Q}^*(\mathcal{M})$, were built by applying the described compression algorithm on each NM with $\mathrm{R}_{\mathrm{m}}^{(1)} = 1.1$ and $\delta_{\mathrm{Marg}}^{(1)} = 0.01$(see Supplementary Information S1). To obtain the VOP set $\boldsymbol{Q}_N^*$ for a particular VOP basis $\boldsymbol{\mathcal{G}}_{\mathrm{VOP}_N} = \{\mathcal{M}_1, \cdots, \mathcal{M}_N\}$, we then applied the same CO algorithm on the union of the model-specific VOPs $\{\boldsymbol{Q}^*(\mathcal{M}_{\mathrm{j}}), 1 \leq j \leq N\}$, this time with $\mathrm{R}_{\mathrm{m}}^{(2)} = 1.1$ and $\delta_{\mathrm{Marg}}^{(2)} = 0$. The above two-stage compression was practical to reduce the computations during the analysis since pre-compression of each individual NM was performed only once for all VOP bases. This approach also appeared to be necessary to reduce the memory demand which scales with N. The VOP matrices for all 64 models, $\boldsymbol{Q}_{64}^*$, were also computed using a similar two-stage approach, and used for the subsequent analyzes.

For each $(\boldsymbol{\mathcal{G}}_{\mathrm{VOP},N}, \boldsymbol{\mathcal{G}}_{\mathrm{TEST}})$ pair, after the construction of the VOPs $\boldsymbol{Q}_N^*$, we computed i) $\mathrm{Rmax}(\mathcal{M}_{\mathrm{TEST}}, \boldsymbol{Q}_N^*)$ and $\mathrm{RiskMass}(\mathcal{M}_{\mathrm{test}}, \boldsymbol{Q}_N^*)$ on every model $\mathcal{M}_{\mathrm{TEST}}$ in $\boldsymbol{\mathcal{G}}_{\mathrm{TEST}}$, ii) gRmax and gRiskMass on the ensemble of the test models, and iii) corresponding sASF(N) and rASF(N). Based on those results, we analyzed sASF and rASF (15 evaluations per each N) as functions of the VOP basis size. We determined their convergence speed as N grows by fitting the data points with the model $\mathrm{ASF}(N) = 1 + \mathrm{A} \cdot N^{-\mathrm{b}}$. This model accounts for the fact that the anatomical safety margins must converge to 1 at $N \to \infty$ as we then cover all possible anatomical variations. To compare the conservativeness of different $\boldsymbol{Q}_N^*$ augmented with obtained ASFs (only rASFs were considered), we calculated the mean VOP-SAR overestimation of the $\mathrm{pSAR}_{10\mathrm{g}}$, $\eta(\boldsymbol{Q}_N^*) = \langle \mathrm{SAR}^*(\mathrm{rASF}(N) \cdot \boldsymbol{Q}_N^*, \boldsymbol{w}) / \mathrm{SAR}^*(\{\boldsymbol{Q_j}; j = 1..64\}, \boldsymbol{w}) \rangle_{\boldsymbol{w}}$, using Monte-Carlo approach with 10^6 random RF shims $\boldsymbol{w}$.

To perform validation on external head models, for all constructed VOP sets $\boldsymbol{Q}_N^*$, we computed the Rmax and RiskMass metrics on the SAR matrices simulated from the Thelonius and Billie models (with error propagation from Eq. 15 included).

The VOP computation algorithm was implemented in Python (3.8.10) using the scipy.optimize module (1.10.1). The computations were performed on the CEA-CCRT supercomputer Topaze (https://www-ccrt.cea.fr/fr/moyen_de_calcul/index.htm), which provides 864 compute nodes with 2x64-cores AMD Milan@2.45GHz (AVX2), 2 GB per core,

256 GB per node. The VOP compression and further evaluation of the R criterion for test models were parallelized on 128 cores. 105 VOP compressions and testings (for different *N* and repetitions) were launched in parallel on 105 nodes.

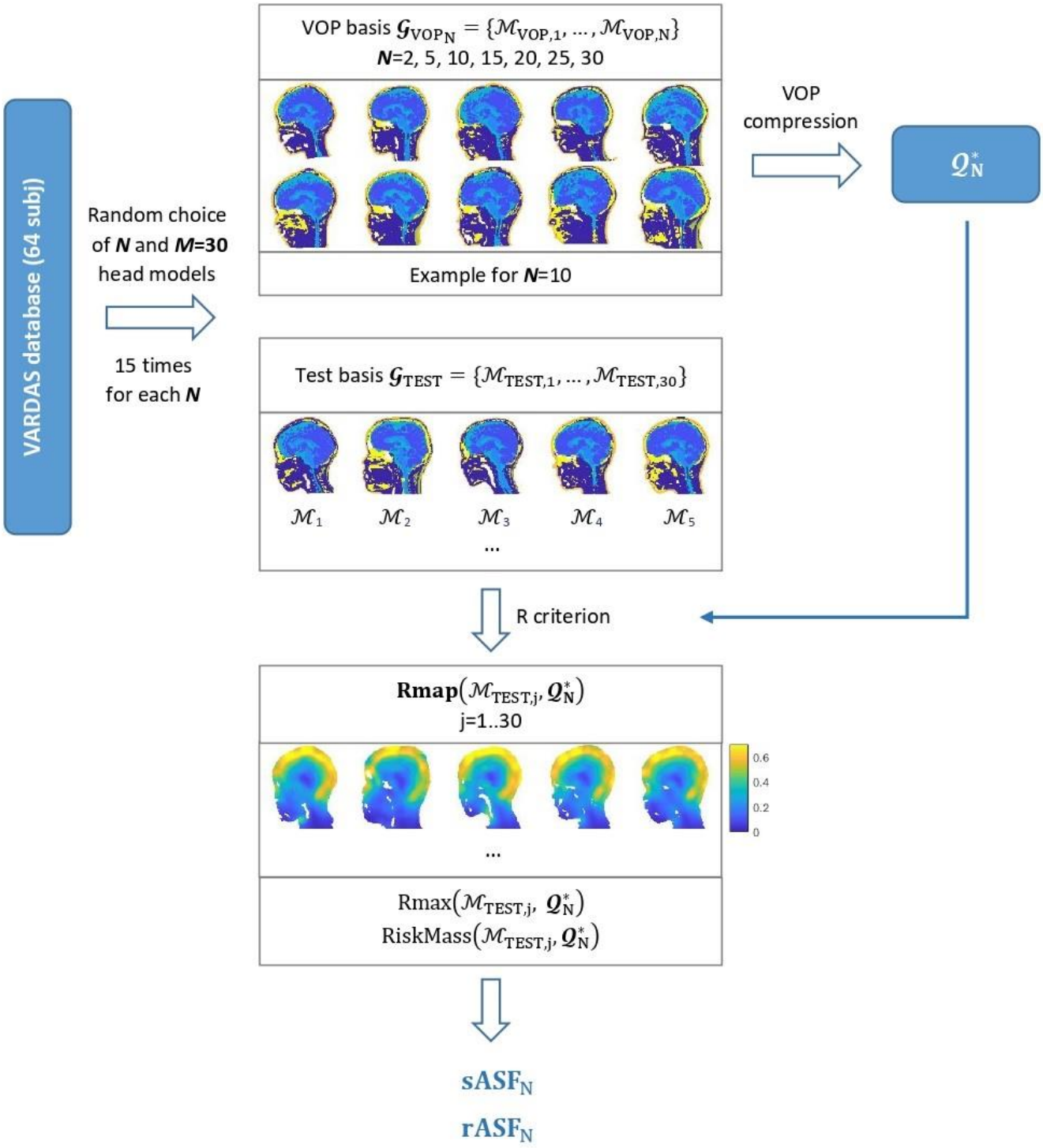

Figure 4. VOP test workflow.

We select N models amongst 64 (the entire VARDAS database) to form the "VOP basis" $\mathcal{G}_{VOP_N}$, and a non-intersecting "TEST basis" of 30 models $\mathcal{G}_{TEST}$. For each test model from $\mathcal{G}_{TEST}$, we compute Rmap, and then Rmax and RiskMass. We then derive sASF and rASF using Eq. 12 and Eq. 13 respectively. This procedure is repeated for N = 2 … 30. For each value of N, a random choice of $\mathcal{G}_{VOP_N}$ and $\mathcal{G}_{TEST}$ is repeated 15 times. The models are chosen randomly but with a condition for sampling the entire age distribution.

4. Results

The boxplots of Fig. 5 show the distributions obtained for test model-specific Rmax and RiskMass values versus the VOP basis size *N***.** For each *N*, repetitions were pooled together, resulting in 450 points (30 test models times 15 repetitions). Fig. 6A shows the mean and the standard deviation of ASF and rASF across 15 repetitions with different $\boldsymbol{\mathcal{G}}_{\mathrm{VOP},N} - \boldsymbol{\mathcal{G}}_{\mathrm{TEST}}$ pairs as a function of *N*. The power-law fits, superimposed on the same graph, returned $s\mathrm{ASF}(N) = 1 + 6.23 \cdot N^{-0.70} (\mathrm{R}^2 = 0.95)$ and $\mathrm{rASF}_N = 1 + 5.37 \cdot N^{-0.75} (\mathrm{R}^2 = 0.93)$. The number of VOP matrices, provided in Fig. 6B, increased slightly with *N* (due to the applied Rmax cutoff in the CO), but systematically. For *N*=2, the number of VOPs ranged from 121 to 193 across all repetitions, and for *N*=30, their number was 218 to 322. Table II shows the calculated and interpolated ASF values. For the VOPs constructed on the entire VARDAS database of 64 models (278 VOP matrices), the power-law interpolants returned for sASF(64) = 1.35 and rASF(64) = 1.24, which correspond to safety factors considering an infinite number of subjects. The relaxed ASF, associated with the tissue mass that is potentially overexposed (existence of pTx RF waveforms were the VOP-SAR underestimates the SAR_{10g}) allows reducing the safety factors by ~10%. The mean overestimation factors $\eta(\boldsymbol{Q}_N^*)$ of the pSAR_{10g} across all 64 models with rASF-augmented VOPs for 10^6 RF shims are provided in Table II. The average value was taken over all RF excitations and over 15 repetitions for each *N*. As hypothesized, the VOP-SAR overestimation decreases with increasing VOP basis size, indicating that $\mathrm{rASF}(N) \cdot \boldsymbol{Q}_N^*$ become less conservative as *N* increases.

In Figure 7, we report the Rmax and RiskMass evaluation on the Thelonius and Billie models. For both models, the strict and the relaxed ASFs are sufficient to ensure VOP safety. Figure 8 shows how the general R distribution evolves for the same test model when testing different VOPs. There, we provide R-maps obtained on one VARDAS model (6 year-old subject), Thelonius and Billie, for two different VOP sets obtained from VOP bases with N=2 and N=30. The results demonstrate a systematic decrease in R value with increasing N for all three models.

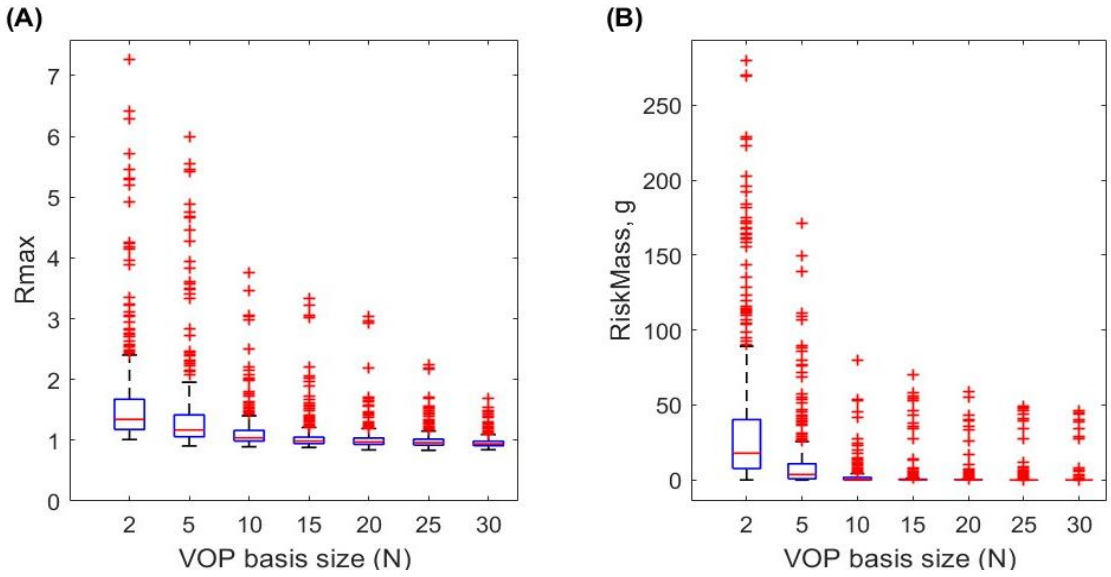

Figure 5. Model-specific (A) Rmax (Eq. 8) and (B) RiskMass (Eq. 9) for test groups $\mathcal{G}_{TEST}$ as a function of the number N of numerical models used to construct VOPs (VOP basis size).

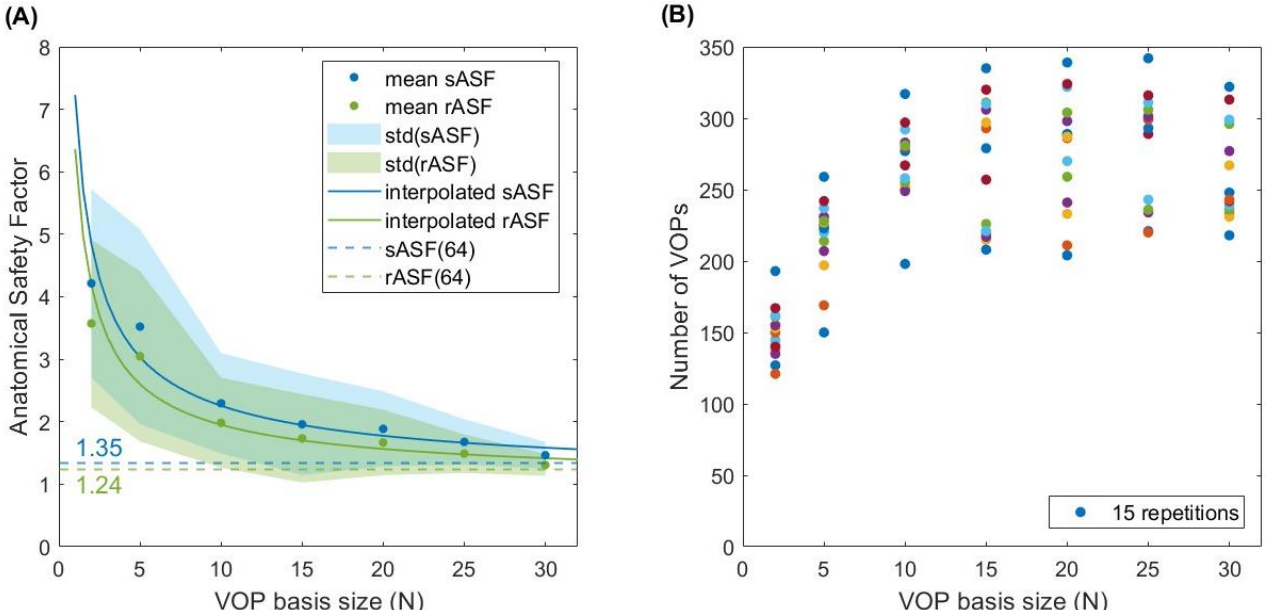

Figure 6. (A): Strict (blue) and relaxed (green) anatomical safety factors (mean and standard deviation across 15 repetitions) plotted as a function of the VOP basis size N. The respective interpolant (power law) are plotted with solid line: $sASF=1+6.23\cdot N^{-0.70}$ ($R^2=0.95$), $rASF=1+5.37\cdot N^{-0.75}$ ($R^2=0.93$). Dash lines represent the safety factors calculated for 64 models. (B): Number of the resulting VOPs vs N for 15 repetitions (each point in a column represents one repetition).

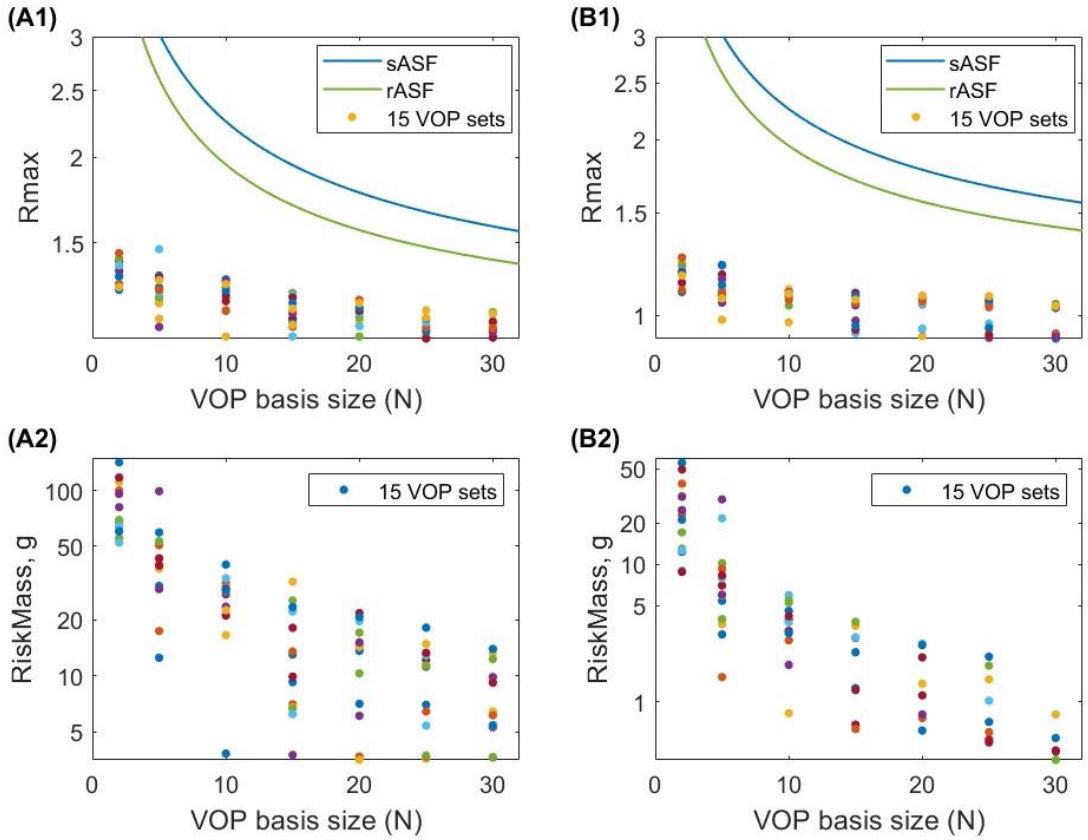

Figure 7. Plot of Rmax (top) and RiskMass (bottom) for Thelonius (A1 and A2) and Billie (B1 and B2) models as a function of N (15 sets of VOP matrices per N, each point in a column represents one repetition). The data are shown in a semi-logarithmic scale.

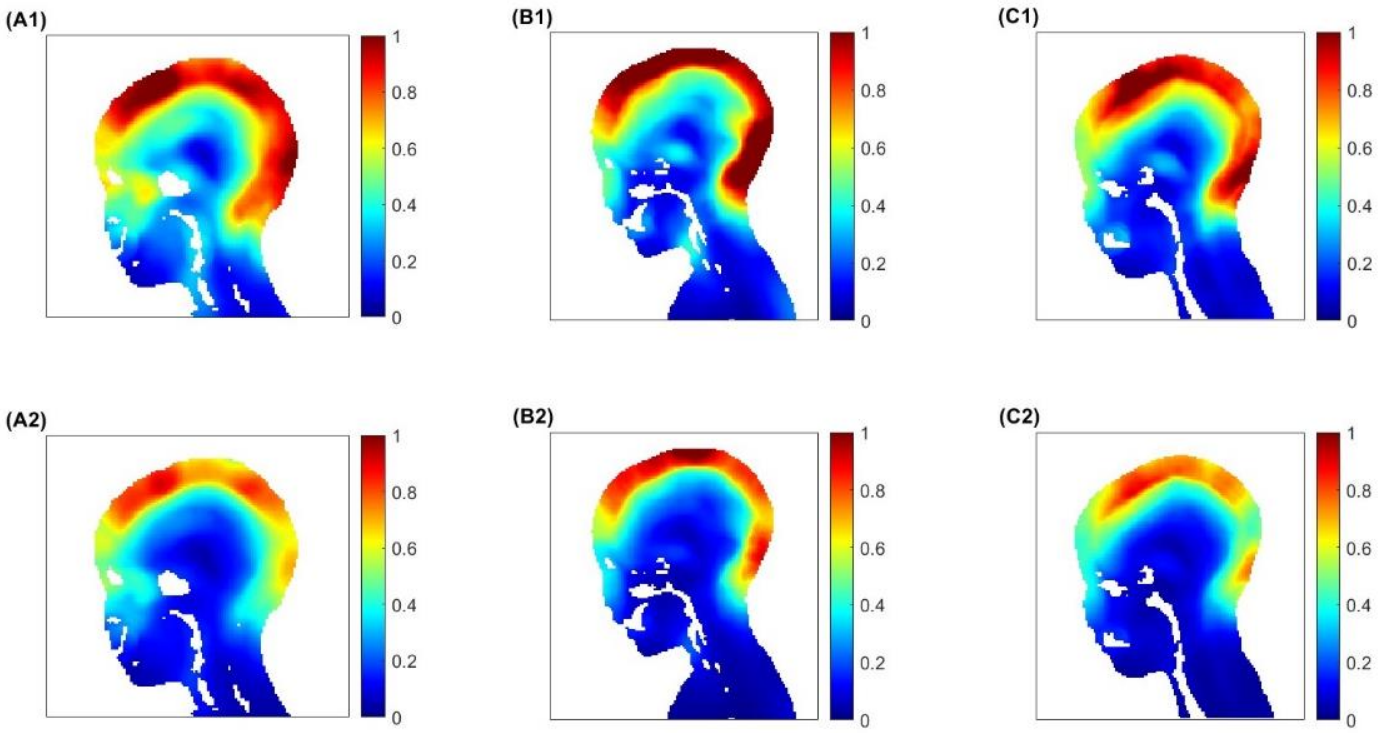

Figure 8. R-maps calculated with VOPs $\boldsymbol{Q}_2^*$ corresponding to the VOP basis size N=2 (upper plots A1, B1, C1) and with $\boldsymbol{Q}_{30}^*$ corresponding to N=30 (lower plots A2, B2, C2). Three models are shown: (A1, A2) one NM from the VARDAS database (6 years, 21.4 kg), (B1, B2) Thelonius and (C1, C2) Billie.

Table II. Estimated (mean ± std) anatomical safety factors (ASF) and their interpolated values versus VOP basis size N as well as the average $pSAR_{10g}$ overestimation by VOPs $\eta(\boldsymbol{Q}_N^*)$. The reported standard deviations are calculated over 15 repetitions. sASF: strict anatomical safety factor; rASF: relaxed anatomical safety factor; $sASF(N) = 1 + 6.23 \cdot N^{-0.70}$; $rASF(N) = 1 + 5.37 \cdot N^{-0.75}$.

N	**2**	**5**	**10**	**15**	**20**	**25**	**30**	**64**
sASF	4.22 ±1.50	3.52 ±1.56	2.30 ±0.80	1.96 ±0.81	1.89 ±0.60	1.68 ±0.36	1.46 ±0.21	-
sASF(*N*)	4.85	3.03	2.26	1.95	1.78	1.66	1.58	1.35
rASF	3.57 ±1.34	3.05 ±1.36	1.98 ±0.72	1.73 ±0.71	1.67 ±0.52	1.49 ±0.31	1.31 ±0.17	-
rASF(*N*)	4.19	2.60	1.95	1.70	1.57	1.48	1.42	1.24
$\eta(\boldsymbol{Q}_N^*)$	3.42±0.29	2.43±0.34	1.85±0.16	1.81±0.25	1.63±0.19	1.60±0.19	1.61±0.17	1.52

5. Discussion

In this study, we addressed the problem of designing VOPs to monitor the peak local SAR in a pediatric exam with pTx. We considered a SAR_{10g} prediction model (VOPs) taking into account the anatomical variability for children above 6 years. We based our analysis on the computation of the worst-case local SAR to VOP-SAR ratio maps, or R-map, which relies on the numerical resolution of a convex optimization problem. This approach does not depend on the specific RF excitation, and thus tackles the major complexity of pTx SAR analysis and overcomes the limitations of Monte-Carlo simulations in a high dimensional space. From the computed R-maps, we extracted simple metrics such as its maximum value or the risk mass and determined quantitatively the minimum required anatomical safety margins to enforce VOP safety.

We analyzed these safety factors depending on the VOP basis size, i.e. the number of models used to compute the VOPs. As the VOP basis increases, the required ASF decreases systematically, as does its standard deviation (See Fig. 6). At the same time, the mean SAR_{10g} overestimation with the rASF-augmented VOPs (η in Table II) also decreases with larger VOP bases. This means that the VOP conservativeness, resulting from the opposite impacts of a larger VOP basis size and a smaller ASF, has a general tendency to decrease with increasing N (while the risk of underestimating SAR_{10g} remains low). The η values demonstrate that for a sufficiently large database used to construct VOPs, the overestimation remains reasonable (η=1.6 starting from 20 models), justifying the use of general rather than subject-specific VOPs (Brink *et al* 2022) in pediatric studies.

For a small VOP basis size, we observed that an "unlucky" choice of the VOP basis can provide R hotspots with values higher than 3 leading to very conservative safety margins. The practical impact of using only a few models would be a severe limitation in the duty-cycle and/or flip angle, or suboptimal pTx excitation for given protocol settings. Hence, in our case, at least N = 10 models are recommended to construct pediatric VOPs with a safety factor of 2; going up to 30, the required ASF drops to 1.4.

Previously reported works such as (Le Garrec *et al* 2017) and (Meliadò *et al* 2020), addressing the SAR inter-subject variability in pTx, mainly base their analysis on Monte-Carlo approach using multiple RF excitations and look at the actual SAR value to estimate the probability to exceed it. In the current study, we introduce a method that considers the risk of the SAR_{10g} underestimation with VOP-SAR and provides its worst-case value amongst all RF

excitations. In this way, we eliminate the source of uncertainty associated with the pTx waveforms. The ASF obtained in our analysis is higher than that usually reported for the head (less than 2) even for a single generic model used for the SAR control. This can be explained, firstly, by our worst case analysis as opposed to usual Monte-Carlo simulations. Additionally, previous studies for pTx have only considered adult models, for which the variation is less compared to the pediatric population. In our work, we used a larger database than those usually available, which encompasses more geometry and positions variations. Indeed, the work (Kopanoglu *et al* 2020), where the authors consider a large range of position changes for one model, reports higher $pSAR_{10g}$ variation reaching a factor of 3. However, despite all of the above, the ASF for large *N* are still comparable to the factors found earlier for adults.

Given potential sources of inaccuracies of the performed simulation (e.g., in segmentation and modelling), we think that the RiskMass metric (counting the voxels in the R-map where R > 1) offers a more relevant way of assessing the SAR_{10g} underestimation risk than the Rmax metric which may correspond to distinct outlier values. Note that the relaxed condition (Eq. 13 a,b) corresponds to the authors' choice (e.g. the RiskMass of 1g ensuring that less than 0.05% of head voxels are at risk for the worst-case RF excitation) and should be seen as a suggestion. We believe that the proposed relaxed condition remains safe especially taking into account the additive systematic SAR_{10g} overestimation with RF power term (Eq. 14) accounting for unavoidable modelling inaccuracies. We note also that the R-criterion reflects a worst-case scenario which cannot occur simultaneously across the entire volume of interest for one pTx RF pulse.

Our analysis depends to some extent on the compression parameters R_m, δ_{Marg}. Our experience indicates that the parameters R_m and δ_{Marg} are useful to adjust the number of VOPs and the SAR_{10g} overestimation due to the compression. In this work, the compression parameters were chosen to keep a reasonable number of VOPs (several hundreds) and a reasonable computation time (~9 min/128 cores to compute $\boldsymbol{Q}^*(\mathcal{M})$). Another important parameter is the factor Λ (Eq. 14) accounting for the simulation inaccuracies. Based on a preliminary analysis of the agreement between the simulated and measured transmit B_1^+ field distribution on reference objects, we used a conservative value of $\Lambda = 0.1$. We note however that as Λ increases, the RF power term $\Lambda\|\mathbf{Q}\|_2\|\boldsymbol{w}(\mathrm{t})\|^2$ tends to dominate over the "raw" SAR term $\boldsymbol{w}(\mathrm{t})^H\mathbf{Q}\boldsymbol{w}(\mathrm{t})$, making the resultant SAR matrix $\mathbf{Q} + \Lambda\|\mathbf{Q}\|_2\mathbf{I}$ merely an RF power monitoring matrix. In this case, the proposed analysis is of little interest since the local SAR becomes proportional to the applied RF power, like in sTx.

Testing the constructed VOPs on standard children models (Thelonious and Billie) revealed the same behavior of safety metrics, i.e. a clear decrease in Rmax and RiskMass with increasing VOP basis size. Application of the previously calculated anatomical safety factors provides VOP-SAR values that effectively overestimate the local SAR for both models.

The VOPs obtained for 64 models and augmented with the calculated rASF will be used in further pediatric studies with the Avanti2 coil after calibrating the simulation results with $\mathbf{L}_{\mathrm{cal}}$ (see Section 3.3). To validate the final VOPs experimentally, we performed thermometric studies on a phantom mimicking the dielectric properties of the tissues (Zanche *et al* 2022). This involved monitoring the temperature rise while playing common protocol sequences with relevant RF pulses designed under the VOP constraints (Gras *et al* 2017). Another test was performed with the RF shim $\boldsymbol{w}$, delivering the maximum transmitted RF power at the maximum allowed $\mathrm{SAR}^{*}(\boldsymbol{Q}^{*}, \boldsymbol{w}) = 10W/kg$, applied for 1 ms in a sequence.

The obtained results naturally depend on the transmit array architecture. However, the proposed approach can be easily transferred to other RF coil designs to find specific safety margins. This will require new electromagnetic simulations for the given coil and numerical models; a separate analysis must be performed to assess the simulation inaccuracies. For the Avanti2 coil used, the transmit elements fit close to the head, making the electric field at the periphery fairly sensitive to the position, orientation, and size of the head, and notably to the distance of the head with respect to the resonators. We expect that the ASF is sensitive to the nominal distance of the body to the transmitting elements and tends to decrease when this distance is increased, as in the case of a coil architecture containing an inner receive-only array and an outer transmit-only array.

Our current analysis has some limitations because we used data available from previous clinical examinations. The models in the VARDAS database do not have uniform distribution by age, the predominant age range being 7 to 9 years, which may bias the analysis. For large sizes of the VOP basis (as well as for the test group), we had to pick up more models from this age group to obtain the required total number of models. In addition, we only had access to T_1 weighted anatomical images. Improving the tissue segmentation would require at least a Dixon image for water-fat discrimination, and a UTE image for the segmentation of the bones, and finally a T_2-w image for optimal segmentation of the CSF (Puonti *et al* 2020, Gabel *et al* 2024).

In this study, we focused on the anatomical variability, and other factors influencing SAR_{10g} should be addressed. Even though the large amount of data and the performed 10-g

averaging of Q matrices tend to limit the effect of segmentations errors by providing more conservative margins, the impact of segmentation accuracy and number of tissue types need further investigations. More elaborated segmentation schemes can be used in the future, possibly involving deep learning-based segmentation (Rashed *et al* 2019, Stolte *et al* 2024). Furthermore, beyond the variability in the head morphology, this approach can be used to study more specifically important position changes (translations and rotations). Here we note that the anatomical diversity of our database implies the "natural" position variation given differences in head shape and hence model positioning in the coil.

The impact of variations in tissue conductivity and dielectric permittivity (McCann *et al* 2019, Sasaki *et al* 2022) has not been addressed in this work and deserves additional consideration. This variation can lead to the local SAR change up to 10% (Shao *et al* 2015, Xu *et al* 2009); Wang *et al* 2024 reported the value of 30%. The work of Bottauscio *et al* 2024 performed on 3 T MRI and addressing different sources of SAR_{10g} variation demonstrated that the variation in head anatomy has a predominant effect compared to tissue properties and head position. However, we cannot translate these results to 7 T MRI with pTx, and a dedicated study is needed.

The general change in tissue dielectric properties with age can also be of interest. In this work, constant average values from adult subjects for each tissue type were used, given that we propose a local SAR model for subjects above 6 years. Indeed, up to 2 years, the child's brain tissues are characterized by a significantly higher water content associated with incomplete myelination, leading to a significant difference in tissue properties compared to adults (Mohammed *et al* 2017); at 3 years of age, brain structures already resemble those of adults, and major fiber tracts have formed (Matsuzawa et al 2001). We can also mention the study of Malik *et al* 2022, conducted for 7 T MRI and a birdcage coil, where the SAR analysis is performed on child models with age-dependent tissue dielectric properties estimated from the water content (Wells et all 2005). The authors concluded that the SAR variation due to using children's dielectric properties instead of adults' was <5%, and that, given different sources of uncertainty (e.g. up to 10% in determining tissue properties), accounting for age-dependent dielectric properties was not necessary in this case.

In the context of the proposed approach, the same cross-validation analysis could be performed for multiple sources of SAR variation (e.g., head position and tissue dielectric properties). The most significant factors to be considered can be identified through an analysis

performed on numerical models in many random configurations (position shifts, rotations, and changes in ε_r and σ), for example by using the Sobol index.

The most significant factors can be identified by performing an analysis on numerical models in many random configurations (position shifts, rotations, changes in εr and σ), for example using the Sobol index, and taken into account.

Finally, using large SAR simulation databases opens the possibility to classify models by age, weight, or head size and to compute for each class a specific set of VOP matrices. This approach could be useful to decrease further anatomical safety factors.

6. Conclusion

We conducted a large-scale numerical study to investigate the VOP safety for pediatric neuroimaging with 7 T MRI in pTx mode, using an in-house developed 16Tx32Rx head coil. We found that using only a few models to compute VOPs requires exceedingly restrictive ASFs (higher than 4 for a VOP basis size of 2) to ensure VOP safety, which would unavoidably lead to pTx performance limitations. We showed that increasing the VOP basis size was useful to reduce the safety factor and to leverage the performance of the coil in transmission. Based on the obtained results, using 30 NHMs to build pediatric VOPs for our system allows us to use an anatomical safety factor as low as 1.4. Although dedicated to a particular setup, it is hoped that this work nevertheless provides a useful general framework to compute VOP matrices and characterize in more details inter-subject variability, with the associated risks, in a pTx-enabled MRI exam.

Acknowledgements

This work was supported the Agence Nationale de la Recherche (ANR) under Grant ANR-21-CE19-0028 (MOSAR) and by the CrossDisciplinary Program on Numerical Simulation of CEA. The work was granted access to the CCRT High-Performance Computing (HPC) facility at CEA under the Grant CCRT2024-dudyshen.

The authors would like to thank Edouard Chazel for his contribution to the coil development, Maya Delbany and Lucie Hertz-Pannier for their contribution to the VARDAS database, and Lucie Hertz-Pannier, Catherine Chiron, and David Germanaud for useful discussions related to the prospect of this work.

Conflict of interest

The authors have no conflict of interest.

References

Adriany G *et al* 2005 Transmit and receive transmission line arrays for 7 Tesla parallel imaging *Magnetic Resonance in Medicine* **53** 434–45

Alushaj E *et al* 2024 Increased iron in the substantia nigra pars compacta identifies patients with early Parkinson's disease: A 3T and 7T MRI study *NeuroImage: Clinical* **41** 103577

Amadon A *et al* 2012 Validation of a very fast B1-mapping sequence for parallel transmission on a human brain at 7T. In proceedings of the 20st ISMRM annual meeting, Melbourne, Australia, Abstract #3358

Annink K V *et al* 2020 Introduction of Ultra-High-Field MR Imaging in Infants: Preparations and Feasibility *American Journal of Neuroradiology*

Balchandani P and Naidich T P 2015 Ultra-High-Field MR Neuroimaging *American Journal of Neuroradiology* **36** 1204–15

Bartolini E *et al* 2019 Ultra-High-Field Targeted Imaging of Focal Cortical Dysplasia: The Intracortical Black Line Sign in Type IIb *American Journal of Neuroradiology* **40** 2137–42

Bartholomeusz H H, Courchesne E and Karns C M 2002 Relationship between head circumference and brain volume in healthy normal toddlers, children, and adults *Neuropediatrics* **33** 239–41

Beqiri A *et al* 2018 Whole-brain 3D FLAIR at 7T using direct signal control *Magnetic Resonance in Medicine* **80** 1533–45

Bottauscio O, Zanovello U, Arduino A and Zilberti L 2024 Polynomial chaos expansion of SAR and temperature increase variability in 3 T MRI due to stochastic input data *Phys. Med. Biol.* **69** 125005

Boulant N *et al* 2018 Workflow proposal for defining SAR safety margins in parallel transmission. In proceedings of the 26th ISMRM annual meeting, Paris, France, Abstract #0295.

Brink W M, Yousefi S, Bhatnagar P, Remis R F, Staring M and Webb A G 2022 Personalized local SAR prediction for parallel transmit neuroimaging at 7T from a single T1-weighted dataset *Magn Reson Med* **88** 464–75

Bubrick E J, Gholipour T, Hibert M, Cosgrove G R, Stufflebeam S M and Young G S 2022 7T versus 3T MRI in the presurgical evaluation of patients with drug-resistant epilepsy *Journal of Neuroimaging* **32** 292–9

Burkett B J *et al* 2021 Clinical 7-T MRI for neuroradiology: strengths, weaknesses, and ongoing challenges *Neuroradiology* **63** 167–77

Caviness V S Jr, Kennedy D N, Richelme C, Rademacher J and Filipek P A 1996 The Human Brain Age 7–11 Years: A Volumetric Analysis Based on Magnetic Resonance Images *Cerebral Cortex* **6** 726–36

Chirita-Emandi A, Doros G, Simina I J, Gafencu M and Puiu M 2015 Head circumference references for school age children in Western Romania *The Medical-Surgical Journal* **119** 1083–91

Christ A and Kuster N 2005 Differences in RF energy absorption in the heads of adults and children *Bioelectromagnetics* **26** S31–44

De Ciantis A *et al* 2016 7T MRI in focal epilepsy with unrevealing conventional field strength imaging *Epilepsia* **57** 445–54

Delbany M *et al* 2022 Variability of the specific absorption rate in the child's head using a transmit array head coil at 7T: a simulation study. In proccedings of the Joint annual meeting of ISMRM-ESMRMB ISMRT 31st Annual Meeting, London, England, UK, Abstract #2552

Destruel A, Jin J, Weber E, Liu F, Guye M and Callot V 2024 On the combination of simulations from various human models to account for variabilities while limiting SAR10g overestimation for UHF pTx MRI. In proccedings of the 2024 ISMRM & ISMRT annual meeting, Singapore, Abstract #3743

Duan C *et al* 2023 Improved visualization of whole-brain structures and pathology at ultra-high field 7T MRI with parallel transmission universal pulses, In proccedings of the 2023 ISMRM & ISMRT annual meeting, Toronto, Canada, Abstract #4229

Dudysheva N, Luong M, Amadon A, Boulant N, and Gras V 2024 Pediatric neuroimaging at 7 Tesla: towards building and validating VOPs for local SAR management in pTX, In proccedings of the 2024 ISMRM & ISMRT annual meeting, Singapore, Abstract #0790

Eichfelder G and Gebhardt M 2011 Local specific absorption rate control for parallel transmission by virtual observation points *Magn Reson Med* **66** 1468–76

Fagan A J, Bitz A K, Björkman-Burtscher I M, Collins C M, Kimbrell V, Raaijmakers A J E and Committee I S 2021 7T MR Safety *Journal of Magnetic Resonance Imaging* **53** 333–46

Feldman R E *et al* 2019 7T MRI in epilepsy patients with previously normal clinical MRI exams compared against healthy controls *PLoS One* **14** e0213642

Fiedler T M, Ladd M E and Bitz A K 2018 SAR Simulations & Safety *NeuroImage* **168** 33–58

Food and Drug Administration; Criteria for Significant Risk Investigations of Magnetic Resonance Diagnostic Devices 2014 https://www.fda.gov/regulatory-information/search-fda-guidance-documents/criteria-significant-risk-investigations-magnetic-resonance-diagnostic-devices-guidance-industry-and

Gabel F, Solomakha G, Bosch D, Glang F, Avdievich N I, Scheffler K and Bause J 2024 Individual voxel models for head SAR estimation

Gabriel C 1996 Compilation of the Dielectric Properties of Body Tissues at RF and Microwave Frequencies.: (Fort Belvoir, VA: Defense Technical Information Center) Online: https://apps.dtic.mil/sti/citations/tr/ADA303903

Goren T, Reboux S, Farcito S, Lloyd B and Kuster N 2024 Influence of patient head definition on induced E-fields during MR examination *Magnetic Resonance in Medicine* **91** 735–40

Gosselin M-C *et al* 2014 Development of a new generation of high-resolution anatomical models for medical device evaluation: the Virtual Population 3.0 *Phys Med Biol* **59** 5287–303

Graesslin I, Homann H, Biederer S, Börnert P, Nehrke K, Vernickel P, Mens G, Harvey P and Katscher U 2012 A specific absorption rate prediction concept for parallel transmission MR *Magnetic Resonance in Medicine* **68** 1664–74

Gras V, Boulant N, Luong M, Morel L, Le Touz N, Adam J-P and Joly J-C 2024 A Mathematical Analysis of Clustering-Free Local SAR Compression Algorithms for MRI Safety in Parallel Transmission *IEEE Trans Med Imaging* **43** 714–22

Gras V, Vignaud A, Amadon A, Le Bihan D and Boulant N 2017 Universal pulses: A new concept for calibration-free parallel transmission *Magn Reson Med* **77** 635–43

Gras V, Wu X and Boulant N 2023 Chapter 7 - Parallel transmission: Physics background, pulse design, and applications in neuro MRI at ultra-high field *Ultra-High Field Neuro MRI* Advances in Magnetic Resonance Technology and Applications (Academic Press) pp 97–123

de Greef M, Ipek O, Raaijmakers A J E, Crezee J and van den Berg C A T 2013 Specific absorption rate intersubject variability in 7T parallel transmit MRI of the head *Magnetic Resonance in Medicine* **69** 1476–85

Hangel G *et al* 2024 Implementation of a 7T Epilepsy Task Force consensus imaging protocol for routine presurgical epilepsy work-up: effect on diagnostic yield and lesion delineation *J Neurol* **271** 804–18

Harris A D, Singer H S, Horska A, Kline T, Ryan M, Edden R a. E and Mahone E M 2016 GABA and Glutamate in Children with Primary Complex Motor Stereotypies: An 1H-MRS Study at 7T *AJNR Am J Neuroradiol* **37** 552–7

Herrler J *et al* 2021 Fast online-customized (FOCUS) parallel transmission pulses: A combination of universal pulses and individual optimization *Magnetic Resonance in Medicine* **85** 3140–53

Herrler J *et al* 2023 The effects of RF coils and SAR supervision strategies for clinically applicable nonselective parallel-transmit pulses at 7 T *Magn Reson Med* **89** 1888–900

Hillyer A, Sharma M, Kuurstra A, Rosehart H, Menon R and Morrow S A 2023 Association between limbic system lesions and anxiety in persons with multiple sclerosis *Multiple Sclerosis and Related Disorders* **79** 105021

IEC 2010 Medical electrical equipment Part 2-33. Particular requirements for the basic safety and essential performance of magnetic resonance equipment for medical diagnosis IEC 60601-2-33 Ed. 3

IEEE 2002 IEEE recommended practice for measurements and computations of radio frequency electromagnetic fields with respect to human exposure to such fields, 100 kHz–300 GHz IEEE C95.3-2002 (New York: IEEE)

Ipek Ö, Raaijmakers A J, Lagendijk J J, Luijten P R and van den Berg C A T 2014 Intersubject local SAR variation for 7T prostate MR imaging with an eight-channel single-side adapted dipole antenna array *Magnetic Resonance in Medicine* **71** 1559–67

Júlíusson P B, Roelants M, Nordal E, Furevik L, Eide G E, Moster D, Hauspie R and Bjerknes R 2013 Growth references for 0–19 year-old Norwegian children for length/height, weight, body mass index and head circumference *Annals of Human Biology* **40** 220–7

Katscher U, Börnert P, Leussler C and van den Brink J S 2003 Transmit SENSE: Transmit SENSE *Magn. Reson. Med.* **49** 144–50

Keith G A *et al* 2024 Towards clinical translation of 7 Tesla MRI in the human brain *IPEM-Translation* **9** 100025

Klodowski K, Zhang M, Scoffings D, Jen J P, Cope T E and Rodgers C T 2024 Parallel transmit (pTx) 7T MRI for drug-resistant focal epilepsy. In proccedings of the 2024 ISMRM & ISMRT annual meeting, Singapore, Abstract #3079

Kopanoglu E, Deniz C M, Erturk M A and Wise R G 2020 Specific absorption rate implications of within-scan patient head motion for ultra-high field MRI *Magn Reson Med* **84** 2724–38

Ladd M E *et al* 2018 Pros and cons of ultra-high-field MRI/MRS for human application *Prog Nucl Magn Reson Spectrosc* **109** 1–50

van Lanen R H G J *et al* 2021 Ultra-high field magnetic resonance imaging in human epilepsy: A systematic review *NeuroImage: Clinical* **30** 102602

Lazen P *et al* 2024 31P MRSI in Pediatric Low Grade Gliomas During Treatment at 7T. In proccedings of the 2024 ISMRM & ISMRT annual meeting, Singapore, Abstract #5081

Le Garrec M, Gras V, Hang M-F, Ferrand G, Luong M and Boulant N 2017 Probabilistic analysis of the specific absorption rate intersubject variability safety factor in parallel transmission MRI *Magnetic Resonance in Medicine* **78** 1217–23

Leitão D *et al* 2022 Parallel transmit pulse design for saturation homogeneity (PUSH) for magnetization transfer imaging at 7T *Magnetic Resonance in Medicine* **88** 180–94

Lenroot R K and Giedd J N 2006 Brain development in children and adolescents: Insights from anatomical magnetic resonance imaging *Neuroscience & Biobehavioral Reviews* **30** 718–29

Luong M, Ferrand G, Chazel E, Gapais P-F, Gras V, Boulant N and Amadon A 2022 A Compact 16Tx-32Rx Geometrically Decoupled Phased Array for 11.7T. MRI Joint Annual

Meeting ISMRM-ESMRMB ISMRT 31st Annual Meeting, London, England, UK, Abstract #0707

Malik S J, Hand J W, Carmichael D W and Hajnal J V 2022 Evaluation of specific absorption rate and heating in children exposed to a 7T MRI head coil *Magnetic Resonance in Medicine* **88** 1434–49

Malik S J, Hand J W, Satnarine R, Price A N and Hajnal J V 2021 Specific absorption rate and temperature in neonate models resulting from exposure to a 7T head coil *Magn Reson Med* **86** 1299–313

Matsuzawa J, Matsui M, Konishi T, Noguchi K, Gur R C, Bilker W and Miyawaki T 2001 Age-related Volumetric Changes of Brain Gray and White Matter in Healthy Infants and Children *Cerebral Cortex* **11** 335–42

McCann H, Pisano G and Beltrachini L 2019 Variation in Reported Human Head Tissue Electrical Conductivity Values *Brain Topogr* **32** 825–58

Meliadò E F, Sbrizzi A, van den Berg C A T, Steensma B R, Luijten P R and Raaijmakers A J E 2020 Conditional safety margins for less conservative peak local SAR assessment: A probabilistic approach *Magnetic Resonance in Medicine* **84** 3379–95

Mohammed B, Jin J, Abbosh A M, Bialkowski K S, Manoufali M and Crozier S 2017 Evaluation of Children's Exposure to Electromagnetic Fields of Mobile Phones Using Age-Specific Head Models With Age-Dependent Dielectric Properties *IEEE Access* **5** 27345–53

Morrison M *et al* 2019 NIMG-56. A multimodal 7 Telsa MRI investigation of long-term effects of radiotherapy on the adolescent brain & cognition *Neuro-Oncology* **21** vi173–4

Myer III C M 1995 Growth of the pediatric skull base: Assessment using magnetic resonance imaging *The Laryngoscope* **105** 1–10

Obusez E C *et al* 2018 7T MR of intracranial pathology: Preliminary observations and comparisons to 3T and 1.5T *NeuroImage* **168** 459–76

Pecqueux B and Labarbe L 2016 Software and hardware assessment of FDTD simulations for very large and complex scenes *2016 International Symposium on Electromagnetic Compatibility - EMC EUROPE* 2016 International Symposium on Electromagnetic Compatibility - EMC EUROPE pp 640–3 Online: https://ieeexplore.ieee.org/document/7739173

Pinho Meneses B *et al* 2022 Shim coils tailored for correcting B0 inhomogeneity in the human brain (SCOTCH): Design methodology and 48-channel prototype assessment in 7-Tesla MRI *NeuroImage* **261** 119498

Puonti O, Van Leemput K, Saturnino G B, Siebner H R, Madsen K H and Thielscher A 2020 Accurate and robust whole-head segmentation from magnetic resonance images for individualized head modeling *NeuroImage* **219** 117044

Rashed E A, Gomez-Tames J and Hirata A 2019 Development of accurate human head models for personalized electromagnetic dosimetry using deep learning *NeuroImage* **202** 116132

Rollins J D, Collins J S and Holden K R 2010 United States head circumference growth reference charts: birth to 21 years *J Pediatr* **156** 907-913.e2

Sasaki K, Porter E, Rashed E A, Farrugia L and Schmid G 2022 Measurement and image-based estimation of dielectric properties of biological tissues -past, present, and future *Phys Med Biol* **67**

Seifert F, Wübbeler G, Junge S, Ittermann B and Rinneberg H 2007 Patient safety concept for multichannel transmit coils *J Magn Reson Imaging* **26** 1315–21

Shao Y, Zeng P and Wang S 2015 Statistical simulation of SAR variability with geometric and tissue property changes by using the unscented transform *Magnetic Resonance in Medicine* **73** 2357–62

Stolte S E *et al* 2024 Precise and rapid whole-head segmentation from magnetic resonance images of older adults using deep learning *Imaging Neuroscience* **2** 1–21

Sun K *et al* 2018 Magnetic resonance imaging of tuberous sclerosis complex with or without epilepsy at 7 T *Neuroradiology* **60** 785–94

Taflove A, Hagness SC 2003 Computational electrodynamics: the finite-difference time-domain method, 3rd ed. Boston, MA: Artech House.

Van Damme L, Mauconduit F, Chambrion T, Boulant N and Gras V 2021 Universal nonselective excitation and refocusing pulses with improved robustness to off-resonance for Magnetic Resonance Imaging at 7 Tesla with parallel transmission *Magnetic Resonance in Medicine* **85** 678–93

van der Plas M C E, van der Voort E C, Wijnen J P and Bhogal A 2024 Strain tensor imaging using single-shot multi-slice DENSE in a pediatric population at 7T. In proccedings of the 2024 ISMRM & ISMRT annual meeting, Singapore, Abstract #2645

Vecchiato K, Casella C, Dokumaci A S, Egloff A, Carney O, Siddiqui A and Jarosz J 2021 High Field 7T MRI in a surgical pediatric epilepsy cohort: a pilot study *American Epilepcy Society*

Veersema T J *et al* 2016 7 Tesla T2*-weighted MRI as a tool to improve detection of focal cortical dysplasia *Epileptic Disorders* **18** 315–23

Veersema T J *et al* 2017 Seven Tesla MRI improves detection of focal cortical dysplasia in patients with refractory focal epilepsy *Epilepsia Open* **2** 162–71

Wang X, Huang S Y and Yucel A C 2024 Uncertainty Quantification in SAR Induced by Ultra-High-Field MRI RF Coil via High-Dimensional Model Representation *Bioengineering* **11** 730

Wells J, Fewtrell M, Davies P, Williams J, Coward W and Cole T 2005 Prediction of total body water in infants and children *Archives of Disease in Childhood* **90** 965

Wolf S, Diehl D, Gebhardt M, Mallow J and Speck O 2013 SAR simulations for high-field MRI: How much detail, effort, and accuracy is needed? *Magnetic Resonance in Medicine* **69** 1157–68

Xu L, Meng M Q-H and Chan Y 2009 Effects of Dielectric Parameters of Human Body on Radiation Characteristics of Ingestible Wireless Device at Operating Frequency of 430 MHz *IEEE Transactions on Biomedical Engineering* **56** 2083–94

Yamada K, Yoshimura J, Watanabe M and Suzuki K 2021 Application of 7 Tesla magnetic resonance imaging for pediatric neurological disorders: Early clinical experience *J Clin Imaging Sci* **11** 65

Yetisir F, Poser B A, Grant P E, Adalsteinsson E, Wald L L and Guerin B 2022 Parallel transmission 2D RARE imaging at 7T with transmit field inhomogeneity mitigation and local SAR control *Magnetic Resonance Imaging* **93** 87–96

Zanche N D *et al* 2022 ISMRM Best Practices for Safety Testing of Experimental RF Hardware, https://doi.org/10.7939/r3-7vpe-x737

Supplementary material

Supplementary information S1

UML diagram of the SAR matrix compression algorithm.

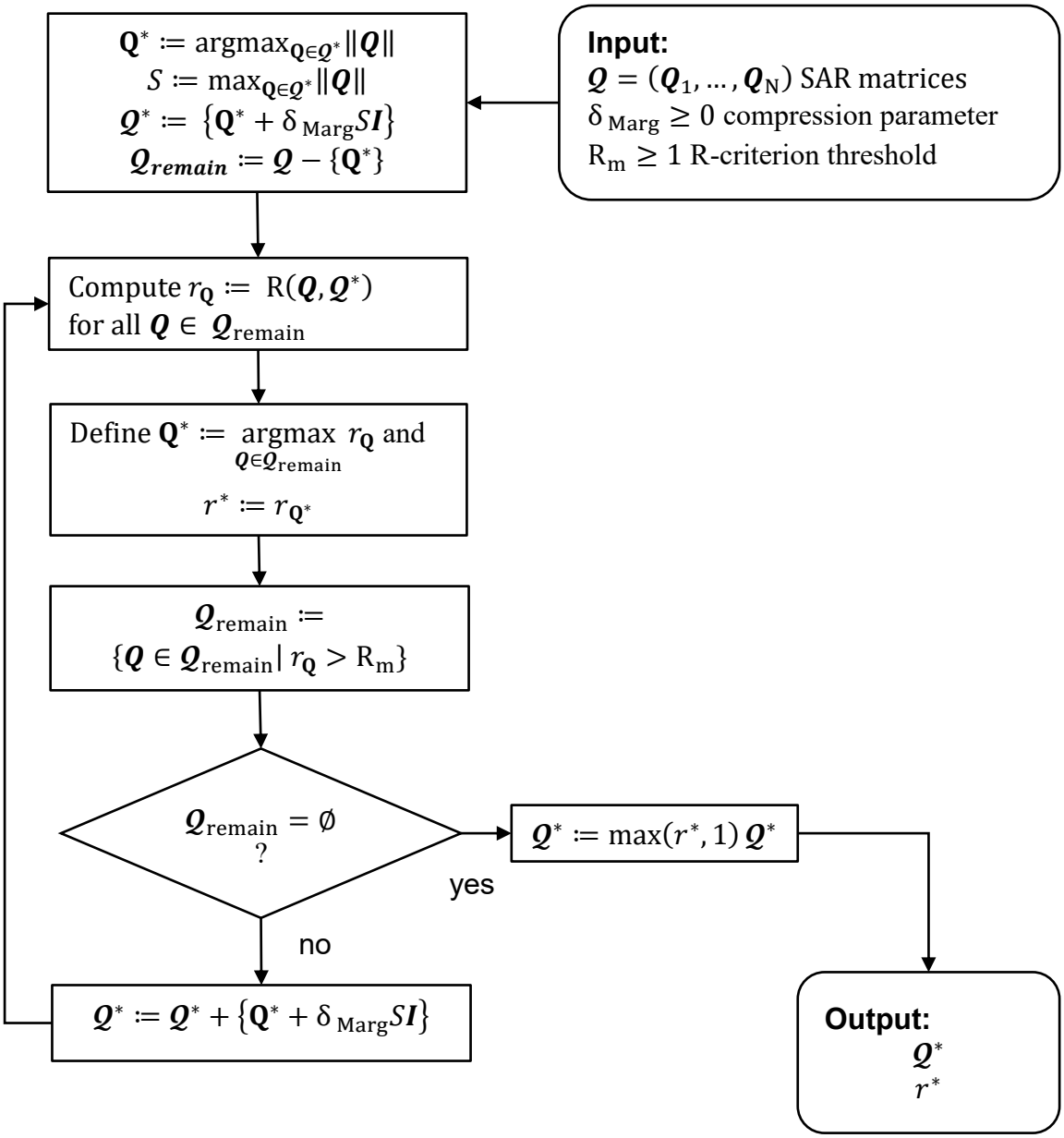

Supplementary information S2

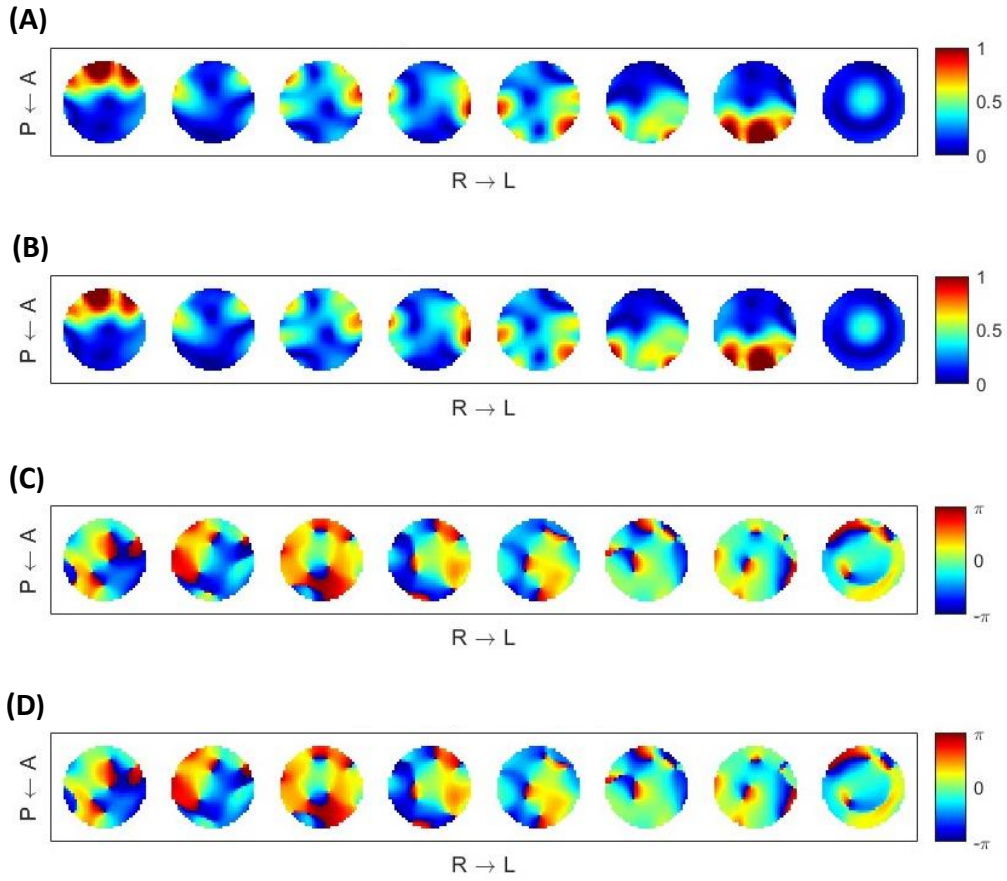

Simulated (A, C) and measured (B, D) B_1^+ maps for the calibration spherical phantom. Images are shown in the median axial plane; (A), (B) – magnitude images, and (C), (D) – phase images. The simulated B_1^+ is shown following the application of the calibration matrix $\mathbf{L}_{cal}$.

Supplementary information S3

Average and standard deviation of B_1^+ and B_1^+ RMS errors (simulation compared to measurement) on each transmission channel after calibration using $\mathbf{L}_{cal}$

channel	**1**	**2**	**3**	**4**	**5**	**6**	**7**	**8**
mean $\lvert B_1^+ \rvert$ (nT/V)	33.2	20.6	29.0	24.0	32.1	26.5	35.8	22.5
σ($\lvert B_1^+ \rvert$) (nT/V)	41.4	14.2	24.8	19.8	27.2	22.2	44.5	22.7
Δ_{rel},%	2.1	1.5	1.7	1.2	1.6	1.2	2.0	1.8

Supplementary information S4

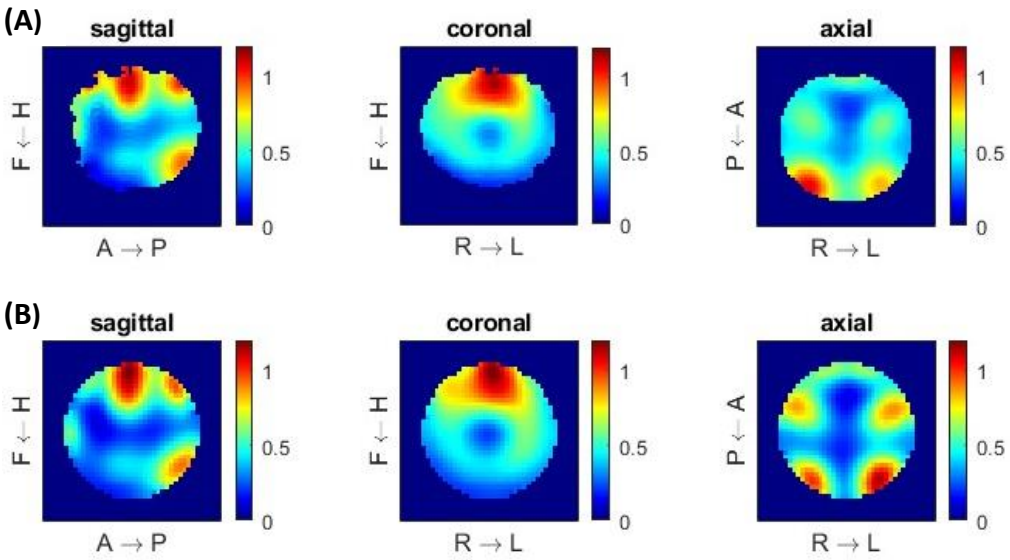

Validation of the electric field simulations using MR thermometry on a spherical gel phantom.

(A) Thermography maps: PRF method, heating during 600 s with a rectangular pulse (CP mode-equivalent drive) of 1 ms and an average power per each channel of 4 W;

(B) Temperature rise predictions based on the SAR simulation and the integration of the heat equation with the following parameters: density 1000 kg/m^3, thermal conductivity 0.5 W/m/K, specific heat capacity 4000 J/K/kg, thermal diffusion coefficient of the gel/air interface 5 m^2/s.

Supplementary information S5

VOP construction workflow

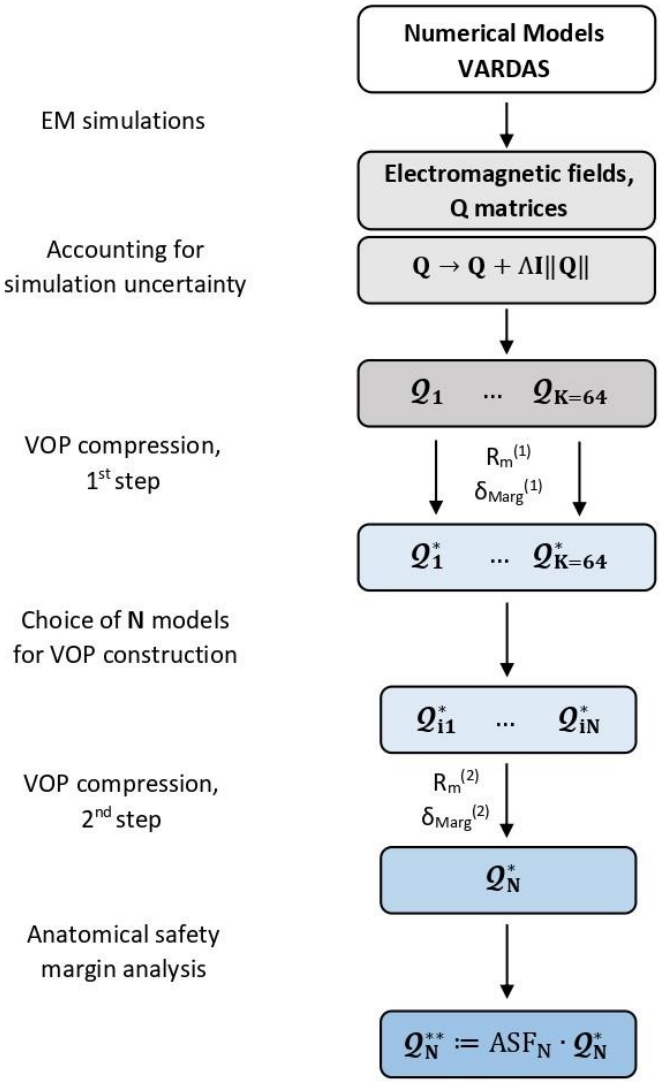

Supplementary information S6

Determination of the calibration error propagation term Λ

In this supplementary material, we describe how we handle a possible discrepancy between the simulated and the actual electromagnetic (EM) field distribution in the head. The general procedure relies on the so-called B_1^+ calibration procedure, described in the first part. Subsequently, we show experimentally that we do not expect this calibration to perfectly correct for simulation biases. Instead, we propose a simple error propagation model ($\mathbf{Q} \mapsto \mathbf{Q} + \Lambda \|\mathbf{Q}\|_2 \mathbf{I}$, i.e. Equation 14) whose role is to upper bound the error in the SAR evaluation due to E-field simulation biases.

B1+ calibration

Due to the specific construction of our coil (dipole pairing), the simulation data consist of 17 EM field simulations (15 dipoles + 1 patch antenna) while the measured data (8-Tx system) consist of 8 measured B_1^+ fields ($\mathbf{B}_{1,\mathrm{meas}}$). The B_1^+ calibration procedure then consists in determining linear combination $\mathbf{L}$ of the simulated B_1^+ fields ($\mathbf{B}_{1,\mathrm{sim}} \mapsto \mathbf{L}\mathbf{B}_{1,\mathrm{sim}}$) that minimize the difference with $\mathbf{B}_{1,\mathrm{meas}}$ (obtained, for example, for a spherical phantom) by solving:

$$\min_{\mathbf{L}} \left\| \mathbf{B}_{1,\mathrm{meas}} - \mathbf{L}\mathbf{B}_{1,\mathrm{sim}} \right\|.$$

Once the calibration matrix $\mathbf{L}$ is determined, we transform the simulated electrical field using the same rule: $\mathbf{E}_{\mathrm{sim}} \mapsto \mathbf{L}\mathbf{E}_{\mathrm{sim}}$ and the SAR matrix according to $\mathbf{Q} \mapsto \mathbf{Q}_{\mathbf{L}} \coloneqq \mathbf{L}^* \mathbf{Q} \mathbf{L}^{\mathrm{T}}$. In Fig. S6-1, we present the calibration matrix obtained on the spherical phantom described in Section 3.3, clearly reflecting the channel pairing strategy. However, in addition to the matrix elements corresponding to the channel pairing and forming a V profile – (1, 1), (1, 15), (2, 2), (2, 14)… (8, 16), (8, 17) – there are other non-null coefficients. This is explained, on the one hand by the absence of the receive array in the simulation (non-accounted coupling), as well other error sources (meshing precision, conductor losses neglected, etc.). As some of these errors affect our ability to predict coupling effects with the sample, we expect the L matrix to be object dependent.

Although this procedure decreases the discrepancies between measurements and simulations (and in our case is necessary to perform the transition 17 Tx → 8 Tx), some sources of uncertainties are still present. Among them, we can name inaccuracies in the B_1^+ mapping method, possible variations in a calibration procedure (optimization, simulation/measurement

alignment, etc.), and finally variations of the **L** matrix with the load, i.e., we expect the calibration matrix obtained on the spherical phantom ($\mathbf{L}_S$) to differ from the one that would be obtained on a subject. We thus repeated the B_1^+ calibration procedure on the two head shaped phantoms (see Fig. S6-1), leading to two "alternative" calibration matrices $\mathbf{L}_C$ (child head) and $\mathbf{L}_A$ (adult head), and compared them with $\mathbf{L}_S$.

Examples of the obtained L-matrices are presented in Fig. S6-1 and calibration results for adult-head phantom are shown in Fig. S6-2. All **L** matrices enabled good correlation between measured and simulated calibrated fields (correlation coefficient >0.97 for each channel). The L matrices for each phantom demonstrated temporal stability across different experimental days. However, comparing the two L matrices corresponding to two different objects reveals greater variations. This is consistent with our expectation that the calibration matrix is, to some extent, load-dependent. In the following, we present a simulation study indicating that the error in the local SAR estimation due to this uncertainty does not exceed $0.1 \times \|\mathbf{Q}\|_2 \|\mathbf{V}\|^2$, where $\boldsymbol{V}$ is the applied RF excitation. We can reach this overestimation by modifying the SAR matrices (before calibration) as $\mathbf{Q} \rightarrow \mathbf{Q} + \Lambda \|\mathbf{Q}\|_2 \mathbf{I}$.

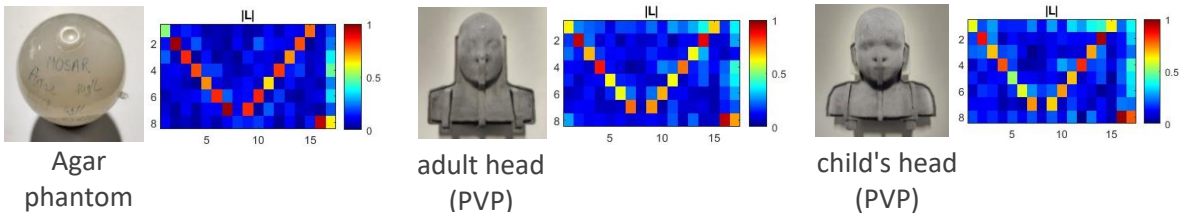

*Figure S1-6. Examples of the calibration matrix **L** for the spherical phantom and two head-shaped phantoms. The V-like profile (columns 1-15) corresponds to the dipole pairing; the matrix elements (8, 16) and (8, 17) correspond to the two ports of the patch.*

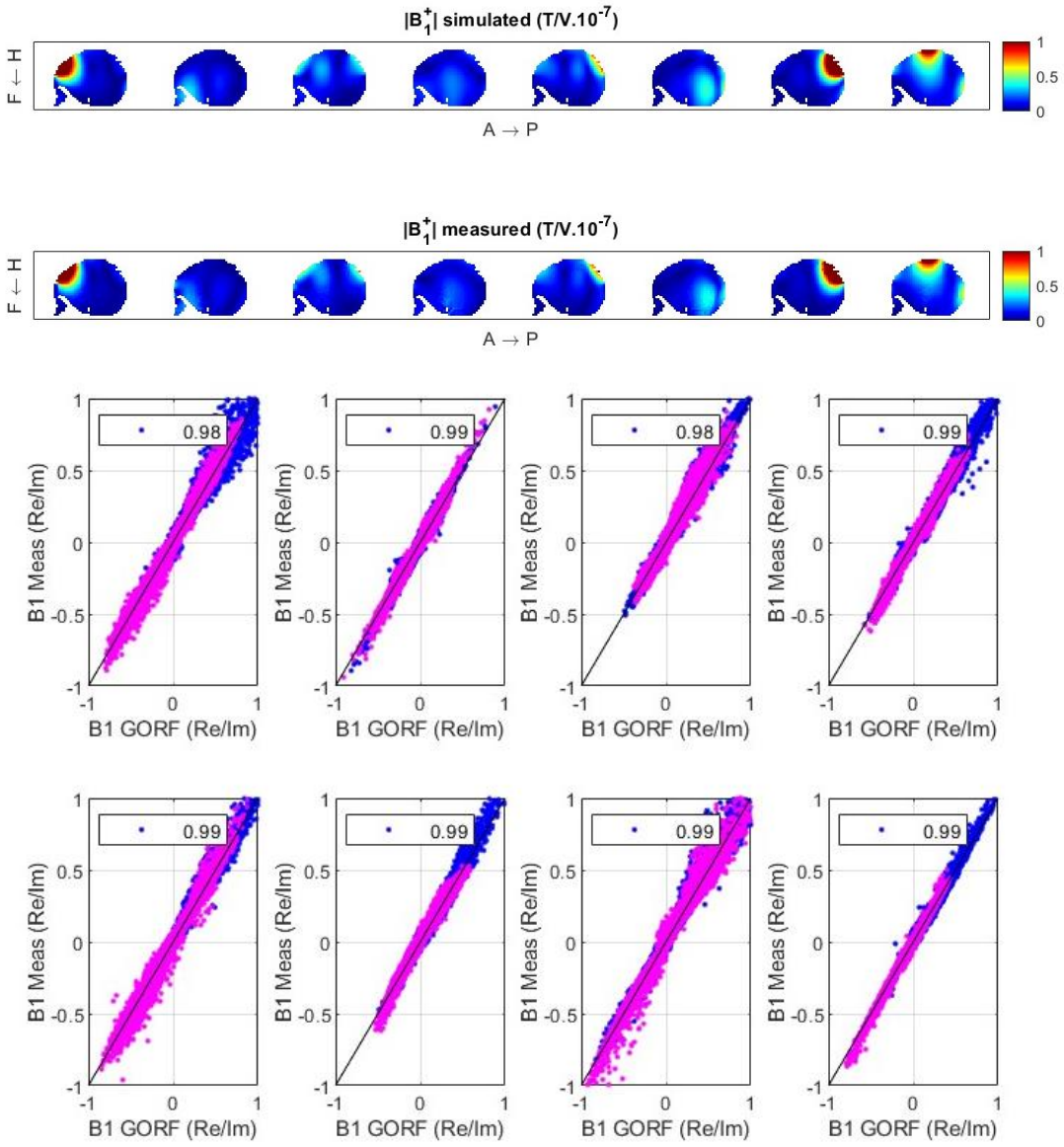

Figure S6-2. Calibration results for the anatomical phantom corresponding to the adult head.

Error propagation benchmark on two models of the IT'IS virtual family

We benchmarked our error propagation model using EM simulation performed on the Thelonius and the Billie models of the IT'IS Virtual Family. We selected 10^4 random RF shims ($\mathbf{V}_i$, $1 \leq i \leq 10^4$) and computed the local SAR for each RF shim using all available calibration matrices (i.e. SAR $= \mathbf{V}_i^H \mathbf{Q}_\mathrm{L} \mathbf{V}_i$ with $\mathbf{L}$ = $\mathbf{L}_\mathrm{S}$, $\mathbf{L}_\mathrm{C}$ and $\mathbf{L}_\mathrm{A}$). At the same time, we computed a "conservative" SAR (cSAR) using the SAR matrices $(\mathbf{Q} + 0.1\|\mathbf{Q}\|\,\mathbf{I})_\mathbf{L}$ with $\mathbf{L}$ = $\mathbf{L}_\mathrm{A}$ and $\mathbf{L}_\mathrm{C}$ (adult and child head phantoms).

In Figures S6-3 and S6-4, we plot peak SAR against peak cSAR (the maximum value across the head for each $\mathbf{V}_i$,) for different calibration scenarios and for the Billie and the Thelonius numerical models respectively. For the cross-validation of the adult head ($\mathbf{L}_\mathrm{A}$) and child head ($\mathbf{L}_\mathrm{C}$) calibration cases in both numerical models, the peak SAR values exceed the peak cSAR value for a maximum of 0.1% of RF shims. As for the calibration based on the spherical phantom ($\mathbf{L}_\mathrm{S}$), we see that in up to 19 % of cases, the peak cSAR does not upper-bound peak SAR. As expected, the difference in loading and the corresponding $\mathbf{L}$ matrices is more significant between the spherical and anatomical phantoms than between the two anatomical phantoms. We also assume that the $\mathbf{L}$ matrix that could correspond to a patient is reasonably closer to that of the adult of child head phantom than that of the spherical phantom.

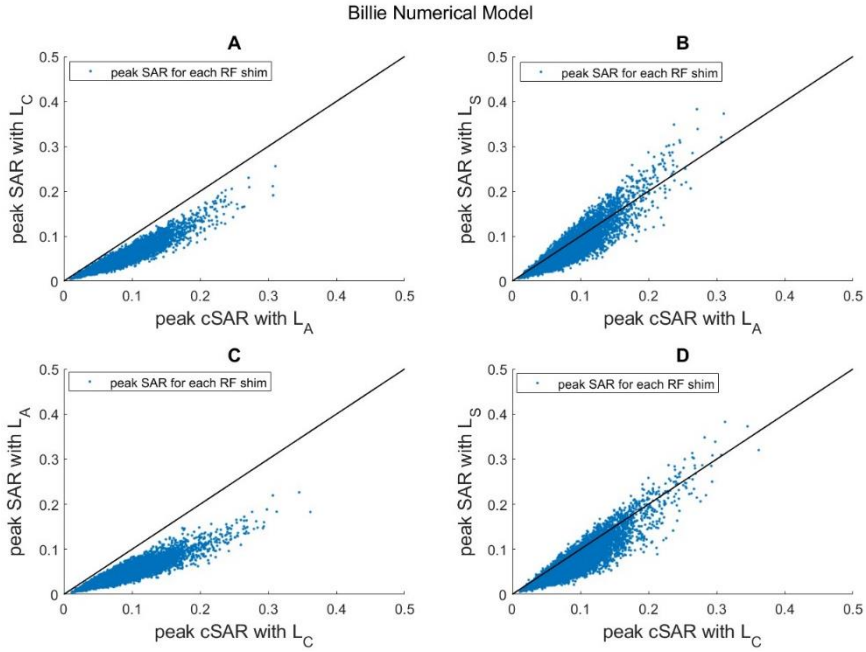

*Figure S6-3. Peak SAR over the head calculated with the Monte-Carlo approach (10^4 random RF shims) using the **Billie** numerical model. X-axis: cSAR calculated with Λ-augmented **Q** matrices (Λ=0.1), Y-axis: SAR calculated with initial **Q** matrices. Different pairs of calibration matrices are used to obtain cSAR and SAR: (A) $\mathbf{L}_A$ and $\mathbf{L}_C$, (B) $\mathbf{L}_A$ and $\mathbf{L}_S$, (C) $\mathbf{L}_C$ and $\mathbf{L}_A$, (D) $\mathbf{L}_C$ and $\mathbf{L}_S$ correspondingly, where $\mathbf{L}_S$ is obtained on the spherical phantom, $\mathbf{L}_A$ – on the adult-head phantom, and $\mathbf{L}_C$ – the on child-head phantom. If the points are below the straight line, the factor Λ=0.1 is sufficient to overestimate SAR variation.*

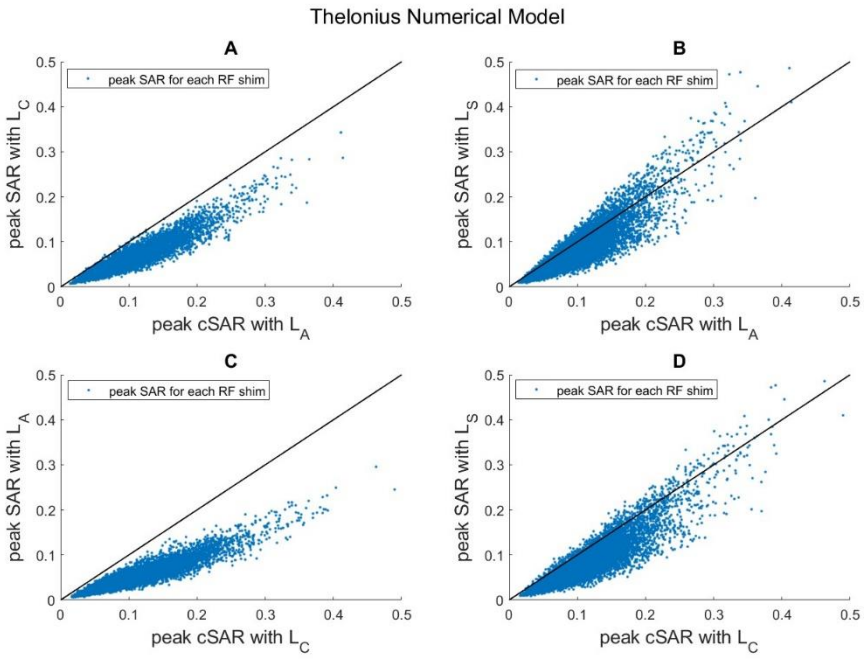

*Figure S6-4. Peak SAR over the head calculated with the Monte-Carlo approach (10^4 random RF shims) using the **Thelonius** numerical model. X-axis: cSAR calculated with Λ-augmented **Q** matrices (Λ=0.1), Y-axis: SAR calculated with initial **Q** matrices. Different pairs of calibration matrices are used to obtain cSAR and SAR: (A) $\mathbf{L}_A$ and $\mathbf{L}_C$, (B) $\mathbf{L}_A$ and $\mathbf{L}_S$, (C) $\mathbf{L}_C$ and $\mathbf{L}_A$, (D) $\mathbf{L}_C$ and $\mathbf{L}_S$ correspondingly, where $\mathbf{L}_S$ is obtained on the spherical phantom, $\mathbf{L}_A$ – on the adult-head phantom, and $\mathbf{L}_C$ – on the child-head phantom. If the points are below the straight line, the factor Λ=0.1 is sufficient to overestimate SAR variation.*

Error propagation benchmark on the VARDAS database

Further, using the VARDAS database, we tested the sufficiency of Λ=0.1 in our pediatric VOP construction to cover the simulation-dependent SAR variations. We took the VOPs made on the 64 VARDAS models with the rASF applied (we remind that the VOPs were constructed on the **Q** matrices augmented with Λ=0.1), and calibrated them with $\mathbf{L}_A$ and $\mathbf{L}_C$ (two sets VOP_{LA} and VOP_{LC}). At the same time, we calibrated all model-specific **Q** matrices with $\mathbf{L}_S, \mathbf{L}_A, \mathbf{L}_C$ (three "Q-matrix scenarios" for each of the 64 models). We then computed the R criterion for each Q-matrix scenario using both VOP_{LA} and VOP_{LC} to check whether the calibrated VOPs cover also the simulation-related SAR variations. The maximum R criterion value for each test model (Fig. S6-5) remains lower 1 for the VOP test on Q matrices corresponding to the $\mathbf{L}_A$ and $\mathbf{L}_C$ scenarios. For the "$\mathbf{L}_S$ scenario" we obtain Rmax > 1 for 4 test models, while RiskMass remains lower than 1 g (0.5g, 0.2g, 0.03g and 0.02g).

In conclusion, this analysis indicates that $\Lambda = 0.1$ used for the pediatric VOP construction covers, in our case, a variation in the calibration matrix that is as large of $\mathbf{L}_S - \mathbf{L}_A$

or $\mathbf{L}_S - \mathbf{L}_C$. To obtain VOPs for in vivo use, we calibrated them with both $\mathbf{L}_A$ and $\mathbf{L}_C$ and concatenated the results (increasing the VOP set size) to further enforce their safety. We note, however, that this calibration uncertainty coefficient of 0.1 is highly related to the specifics of the coil, calibration, and VOP compression procedure. The described procedure should be seen as a proposed way of reasoning to account for the simulation/measurement discrepancies.

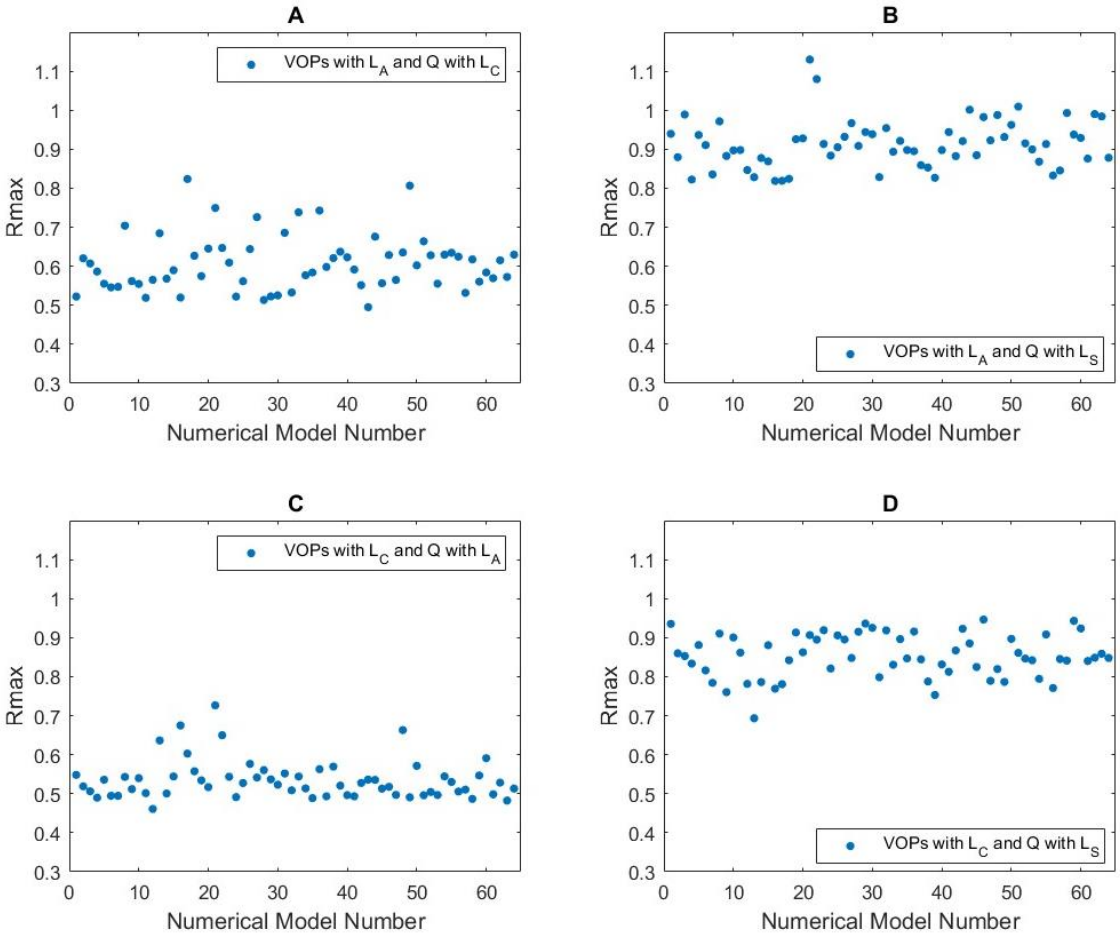

*Figure S6-5. R-criterion test of the VOPs calibrated with one matrix **L** on Q matrices of 64 VARDAS numerical models calibrated with another **L**. Different pairs of calibration matrices are considered: (A) $\mathbf{L}_A$ and $\mathbf{L}_C$, (B) $\mathbf{L}_A$ and $\mathbf{L}_S$, (C) $\mathbf{L}_C$ and $\mathbf{L}_A$, (D) $\mathbf{L}_C$ and $\mathbf{L}_S$. $\mathbf{L}_S$ corresponds to the spherical phantom, $\mathbf{L}_A$ – to the adult-head phantom, and $\mathbf{L}_C$ – to the child-head phantom.*
The maximum R values obtained for each numerical model are presented. Rmax values lower than 1 signify that, for the given model, the VOPs overestimate SAR despite the uncertainty in the L matrix estimation.